



Turbulence Organization and Mean Profile Shapes in the Stably Stratified Boundary Layer: Zones of Uniform Momentum and Air Temperature

Michael Heisel¹ · Peter P. Sullivan² · Gabriel G. Katul³ · Marcelo Chamecki¹

Received: 25 July 2022 / Accepted: 18 November 2022
© The Author(s) 2022

Abstract

A persistent spatial organization of eddies is identified in the lowest portion of the stably stratified planetary boundary layer. The analysis uses flow realizations from published large-eddy simulations (Sullivan et al. in *J Atmos Sci* 73(4):1815–1840, 2016) ranging in stability from near-neutral to almost z-less stratification. The coherent turbulent structure is well approximated as a series of uniform momentum zones (UMZs) and uniform temperature zones (UTZs) separated by thin layers of intense gradients that are significantly greater than the mean. This pattern yields staircase-like instantaneous flow profiles whose shape is distinct from the mean profiles that emerge from long-term averaging. However, the scaling of the staircase organization is closely related to the resulting mean profiles. The differences in velocity and temperature across the thin gradient layers remain proportional to the surface momentum and heat flux conditions regardless of stratification. The vertical thickness of UMZs and UTZs is proportional to height above the surface for near-neutral and weak stratification, but becomes thinner and less dependent on height as the stability increases. Deviations from the logarithmic mean profiles for velocity and temperature observed under neutral conditions are therefore predominately due to the reduction in eddy size with increasing stratification, which is empirically captured by existing Monin–Obukhov similarity relations for momentum and heat. The zone properties are additionally used to explain trends in the turbulent Prandtl number, thus providing a connection between the eddy organization, mean profiles, and turbulent diffusivity in stably stratified conditions.

Keywords Turbulence · Surface layer · Stable stratification · Monin–Obukhov similarity · Large-eddy simulation

✉ Michael Heisel
heisel@ucla.edu

¹ Department of Atmospheric & Oceanic Sciences, University of California Los Angeles, Los Angeles, CA 90095, USA

² National Center for Atmospheric Research, Boulder, CO 80301, USA

³ Department of Civil and Environmental Engineering and Nicholas School of the Environment, Duke University, Durham, NC 27708, USA

1 Introduction

Since the introduction of Monin–Obukhov (M–O) similarity theory (Monin and Obukhov 1954; Foken 2006), significant effort has been devoted to fine-tuning the empirical similarity relations $\phi(z/L)$ (e.g., Businger et al. 1971; Dyer 1974; Högström 1988). A logarithmic wind profile is expected for neutrally stratified conditions in the planetary boundary layer (PBL), and ϕ accounts for deviations from the logarithmic profile due to thermal stability effects. The basis of the theory is that ϕ is a universal function of z/L for a given dimensionless quantity such as the mean shear, where z is height above the surface and L is the Obukhov length defined using surface scaling parameters (Obukhov 1946). Due to limitations in measuring and simulating atmospheric turbulence, the fine-tuning efforts have not been accompanied by a concrete understanding of how the organization and intensity of turbulent eddies quantitatively changes with varying stratification. Aspects of the eddies can be inferred from various techniques including visualization by fog and clouds (Young et al. 2002), spectra of point measurements (Kaimal et al. 1972), refractive indexing (Wyngaard et al. 2001), correlations across an array of sensors (Salesky et al. 2013; Lan et al. 2018), and integral scales from simulations (Huang and Bou-Zeid 2013; Chinita et al. 2022), but there is scant evidence supporting a formal link between the eddy properties and $\phi(z/L)$ (Katul et al. 2011).

The prevailing organization of turbulent motions depends on the stability regime. These motions have been widely observed in the convective PBL due to the large and long-lived scale of the dominant eddies; the prominence of elongated streaks near the surface in neutral conditions (Young et al. 2002), roll vortices of various sizes in weak convection (Etling and Brown 1993), and open cells dominated by buoyancy in forced convection (Atkinson and Zhang 1996) have all been observed experimentally and with large-eddy simulations (LES) (Khanna and Brasseur 1998; Shah and Bou-Zeid 2014; Patton et al. 2016; Salesky et al. 2017; Jayaraman and Brasseur 2021). Relatively less is known about the organization of turbulent eddies in stably stratified conditions (see Mahrt 2014 for a review on the topic). Average flow statistics reveal distinct scaling regimes for the stable PBL (Holtslag and Nieuwstadt 1986; Mahrt 1999): in the near-surface region under weak stratification, the traditional M–O surface parameterization appears applicable; farther from the surface, similarity is better represented using local, height-dependent fluxes in the definition of L (Nieuwstadt 1984; Sorbjan 1986); under increased stability, the flow approaches z -less stratification for which z is no longer a relevant parameter (Wyngaard and Coté 1972); finally, very stable conditions yield large-scale global intermittency throughout the PBL depth (Mahrt 1989). Simulations for weak stratification at relatively low Reynolds number found turbulent features similar to neutral conditions (García-Villalba and del Álamo 2011; Watanabe et al. 2019; Atoufi et al. 2021). It is reasonable to expect the properties of these eddies to be consistent with scaling of the more stable regimes, e.g., a loss of height dependence in eddy size for z -less stratification, but a detailed assessment relating the turbulent eddy organization and average flow statistics in stably stratified conditions has not been made to date and frames the scope here.

Recent advances in turbulent boundary layer research can be used as a starting point for such an assessment. Instantaneous realizations of neutrally stratified wall-bounded flows can be approximated as a population of large regions of relatively uniform along-wind momentum. These regions are separated by thin layers characterized by enhanced shear and vorticity (Meinhart and Adrian 1995; Priyadarshana et al. 2007). The large regions are known as uniform momentum zones (UMZs) (Meinhart and Adrian 1995; de Silva et al. 2016), and the thin layers associated with the UMZ edges have various descriptors including internal shear layers (Gul et al. 2020), internal interfacial layers (Fan et al. 2019), and vortical fissures (Priyadar-

shana et al. 2007). The intermittent spacing of small-scale features concentrated within the thin layers has been identified for more general flow conditions (e.g., Ishihara et al. 2009) including direct observation in the atmospheric surface layer (Heisel et al. 2018), such that this observed eddy organization is considered a potential archetypal turbulent structure (Hunt et al. 2010; Elsinga and Marusic 2010; Ishihara et al. 2013; Hunt et al. 2014).

The organization of UMZs and shear layers is closely related to the long-studied issue of small-scale (internal) intermittency (Sreenivasan and Antonia 1997). Enhanced velocity gradients and dissipation values occur in intermittent intervals corresponding to the shear layer positions, leading to probability distributions with long tails that grow with Reynolds number (Batchelor and Townsend 1949) and favor extreme maximum values relative to the mean (Buaria et al. 2019). The intermittent behavior of dissipation statistics in particular led to the revision of Kolmogorov's original 1941 similarity hypotheses (Obukhov 1962; Kolmogorov 1962). While there are now numerous mathematical models to account for small-scale intermittency in statistics (see, e.g., Frisch et al. 1978; Meneveau and Sreenivasan 1991), a direct and quantitative connection to the organization of eddies is a topic of ongoing work (Elsinga et al. 2020).

The UMZs and shear layers are also related to previously identified features because the generic definition of UMZs applies to any coherent velocity region. For example, the signature of UMZs in the inertial layer corresponds closely to low-momentum streaks that are often sandwiched by high-momentum counterparts (Hutchins and Marusic 2007; Dennis and Nickels 2011; Smits et al. 2011). These streaks have been observed for atmospheric flows using arrays of point sensors (Wilczak and Tillman 1980; Hutchins et al. 2012), Doppler lidar (Träumner et al. 2015), and large-eddy simulations (Salesky and Anderson 2018). The low-momentum streaks—and the signature of a UMZ—have been associated with packets of hairpin-like vortices aligned with the high-shear region along the upper edge of the UMZ (Adrian et al. 2000; Adrian 2007). Similar vortical features have been identified in measurements (Hommema and Adrian 2003; Carper and Porté-Agel 2004; Hutchins et al. 2012; Heisel et al. 2018) and LES (Lin et al. 1996) of atmospheric flows. A key advantage of detecting UMZs and their edges as opposed to streaks and hairpin-like vortices is that it allows for a quantitative link between eddy organization and mean flow statistics. For instance, in neutral conditions the characteristic velocity of the shear layers is the friction velocity u_* and the vertical thickness of UMZs is proportional to z (Heisel et al. 2020). These parameters match the behavior assumed in derivations of the logarithmic (log) law such as Prandtl's mixing length closure (Prandtl 1932) and Townsend's attached eddy hypothesis (Townsend 1976), thus identifying the organization of eddies in physical space underlying the logarithmic wind profile that forms the foundation of M-O similarity. Simplified models based on these eddy properties can reproduce the first- and higher-order flow statistics for canonical boundary layers (de Silva et al. 2017; Marusic and Monty 2019; Bautista et al. 2019).

The same organization of eddies has been proposed for the turbulent temperature field in stratified conditions, namely uniform temperature zones (UTZs) and thin layers with concentrated temperature gradients (Ebadi et al. 2020). These thin gradient layers have been observed in simulations of stably stratified shear turbulence (Chung and Matheou 2012; Glazunov et al. 2019) and are traditionally known as fronts (Chen and Blackwelder 1978; Sullivan et al. 2016) or microfronts (Mahrt and Howell 1994; Mahrt 2019) separating regions of differing temperature. Similar to the thin shear layers, hairpin-like vortices have been detected along the fronts (Mahrt and Howell 1994; Sullivan et al. 2016). It is likely that the fronts are related to the cliffs of the ramp-cliff pattern common in time series of temperature and other scalars (Antonia et al. 1979; Kikuchi and Chiba 1985; Warhaft 2000). Further, the persistent presence of the fronts and ramp-cliff structure yields a staircase-like shape in

instantaneous profiles of the temperature (Sullivan et al. 2016). The layering of the turbulent eddies and the corresponding stairstep profile have been observed for stratified flows in applications beyond the atmosphere (see, e.g., Praud et al. 2005; Basak and Sarkar 2006; Waite 2011; Caulfield 2021 and references therein). These patterns are analogous to the stairstep profile of UMZs and shear layers seen for velocity (de Silva et al. 2016; Heisel et al. 2020). Hence, the UMZ framework can similarly be applied to the temperature field to quantify the vertical thickness of UTZs (i.e., vertical spacing between fronts) and the intensity of the temperature difference across the front to relate the turbulent temperature structure to the mean profile.

The present work uses existing techniques for detecting UMZs and UTZs to investigate the organization of turbulent eddies in the stably stratified PBL. Turbulent flow volumes are analyzed from a previously published suite of high-resolution LES (Sullivan et al. 2016). The LES conditions range from near-neutral to almost z-less stratification and exclude the very stable regime with global intermittency. The region of interest is the lower portion of the PBL including heights within and closely above the surface layer where a transition from surface to local to z-less scaling is expected. The study seeks to address two key questions motivated by the above introduction: (i) is the organization of turbulent eddies in the stably-stratified PBL qualitatively similar to neutral conditions (i.e., a series of UMZs and UTZs)? (ii) how do changes in the eddy properties with increasing stratification relate to log law mean profile deviations that are predicted empirically by $\phi(z/L)$? The remainder of the article is organized as follows: the LES and detection of uniform zones are detailed in Sect. 2; properties of the detected zones are presented in Sect. 3; concluding remarks are given in Sect. 4.

2 Methodology

The first four subsections provide a detailed account for each aspect of the analysis: simulation of the PBL (2.1), rotation of the numerical grid in post-processing (2.2), detection of UMZs (2.3), and detection of UTZs (2.4). An abbreviated summary of the methodology is given in Sect. 2.5 for readers only interested in the details essential for understanding the results in Sect. 3.

2.1 Planetary Boundary Layer Simulations

The analysis is conducted on previously published LES of the stably stratified PBL (Sullivan et al. 2016). A new simulation for near-neutral stratification is also included here to assess the transition from neutral to stable conditions. A complete description of the stratified simulations (Sullivan et al. 2016) and similar neutral simulations (Moeng and Sullivan 1994; Lin et al. 1996) are provided elsewhere, and an overview of relevant details is given here.

The LES design follows the GEWEX Atmospheric Boundary Layer Study (GABLS) benchmark case for a canonical stable PBL (see, e.g., Beare et al. 2006; Basu and Porté-Agel 2006; Cuxart et al. 2006; Huang and Bou-Zeid 2013; Matheou and Chung 2014). The geostrophic wind ($U_g = 8 \text{ m s}^{-1}$), high-latitude Coriolis frequency ($f = 1.39 \times 10^{-4} \text{ s}^{-1}$), still air initial potential temperature ($\theta_o = 265 \text{ K}$), capping inversion strength (0.01 K m^{-1}), domain size (400 m in each direction), and fixed surface cooling rate ($C_r = 0.25 \text{ K h}^{-1}$) of the benchmark case were all adopted for the present LES. Three additional higher cooling rates up to $C_r = 1 \text{ K h}^{-1}$ were also simulated. The surface heat flux resulting from the imposed cooling was estimated from the difference in temperature between the surface and the first

Table 1 Key scaling parameters for large-eddy simulations (LES) of the near-neutral and stably stratified planetary boundary layer: surface cooling rate C_r , surface heat flux Q_* , friction velocity u_* , surface temperature scaling θ_* , Obukhov length L , capping inversion height z_i , and momentum flux profile depth h . A full account of the stable LES is given elsewhere (Sullivan et al. 2016)

Symbol	C_r (K h ⁻¹)	$Q_* \times 10^3$ (K m s ⁻¹)	u_* (m s ⁻¹)	θ_* (K)	L (m)	z_i (m)	z_i/L (–)	h/z_i (–)
▽	0	0	0.332	0	$O(10^5)$	263	0.0	0.98
○	0.25	–9.63	0.255	0.0378	116	198	1.7	0.81
×	0.375	–11.5	0.234	0.0493	74.7	182	2.4	0.75
△	0.5	–13.5	0.222	0.0607	54.7	173	3.2	0.71
+	1	–19.5	0.194	0.100	25.5	154	6.0	0.58

grid point. The conventionally neutral PBL was modeled using the same flow conditions and a surface heat flux prescribed to be zero. Any buoyancy effects observed within the PBL in this case originate from weak entrainment at the capping inversion. The conditions are hereafter referred to as “near-neutral” in consideration of these weak buoyancy effects seen in later statistics.

The stably stratified LES was computed on a 1024^3 numerical grid, yielding an isotropic resolution $\Delta = 0.39$ m in each direction. The near-neutral conditions were discretized on a relatively smaller 512^3 grid corresponding to $\Delta = 0.78$ m. Consideration of the difference in resolution is discussed in Sect. 2.3. For all cases, the LES employed a two-part subgrid-scale (SGS) model detailed elsewhere (Sullivan et al. 1994). The surface conditions at the bottom boundary were estimated using an M-O similarity wall model (Moeng 1984) evaluated locally using the first point above the surface (Mironov and Sullivan 2016), whose height is $\Delta/2$ on the staggered LES grid.

The scaling parameters resulting from each simulated surface cooling rate are listed in Table 1. Here, $Q_* = \langle w'\theta' \rangle(z=0)$ is the surface heat flux, $u_* = \sqrt{\langle u'w' \rangle_\perp(z=0)}$ is the friction velocity calculated from the surface momentum flux, $\theta_* = -Q_*/u_*$ is the surface temperature scaling, and the Obukhov length definition $L = -u_*^2\theta_0/\kappa g\theta_*$ is based on the von Kármán constant $\kappa = 0.4$ and gravitational constant g . Angled brackets “ $\langle \cdot \rangle$ ” imply averaging across both time and the horizontal plane, prime notations “ $'$ ” indicate fluctuations around the average value, e.g., $u' = u - \langle U \rangle$, and the subscript \perp is shorthand for the magnitude of the horizontal velocity (u and v) contributions, e.g., $\langle u'w' \rangle_\perp = \sqrt{\langle u'w' \rangle^2 + \langle v'w' \rangle^2}$. The virtual potential temperature θ is hereon simplified as “temperature”.

The depth of the PBL is characterized here as the inversion height z_i based on the position where the temperature gradient $\partial\langle\theta\rangle/\partial z$ is maximized (Sullivan et al. 1998). Another common definition for the PBL depth in stable conditions is the height where the average shear stress is a small fraction of the surface value. This depth $h = z(\langle u'w' \rangle_\perp = 0.05u_*^2)/0.95$ (Kosović and Curry 2000) is closely related to the position of the low-level jet (Blackadar 1957). The height z_i is used in the later analysis and results because the turbulence above h is considered to be part of the PBL, noting that the general findings of the study do not depend on whether z_i or h is used for the PBL depth. For the near-neutral LES case, the Obukhov length based on local flux parameters is $L(z) \sim O(10^4 - 10^5)$ in the lowest 10% of the PBL and decreases with height. Top-down buoyancy effects in this case are small compared to stability effects of the remaining cases such that the conditions are considered near-neutral for the purposes of the study. The stable cases (in order of increasing C_r) correspond to runs C, D, E, and F in the original study (Sullivan et al. 2016).

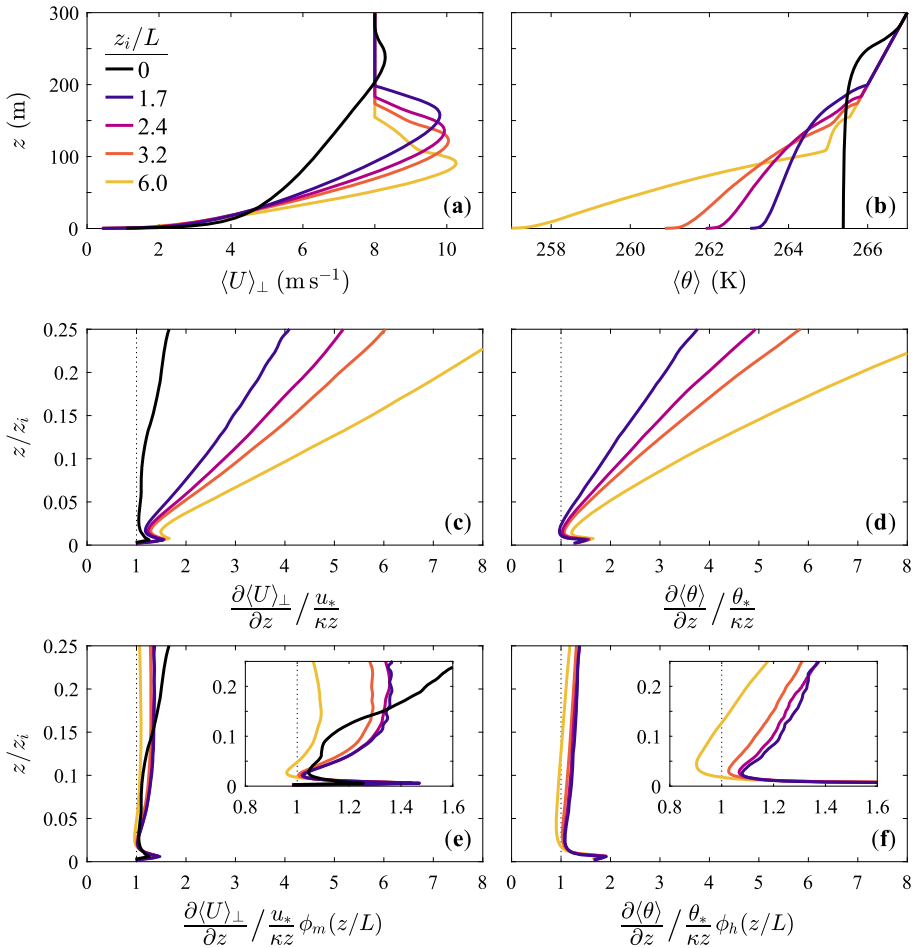


Fig. 1 Mean profiles for the large-eddy simulations (LES) of a stably stratified planetary boundary layer: **a** horizontal wind speed magnitude $\langle U \rangle_{\perp} = \sqrt{\langle U \rangle^2 + \langle V \rangle^2}$; **b** virtual potential temperature $\langle \theta \rangle$; **c** velocity gradient; **d** temperature gradient; **e** velocity gradient with the similarity relation $\phi_m = 1 + 4.7z/L$ for momentum; **f** temperature gradient with the similarity relation $\phi_h = 0.74 + 4.7z/L$ for heat. In this and later figures, the legend corresponds to the z_i/L stability parameter for each LES case in Table 1

Profiles of the mean horizontal wind speed and air temperature are respectively shown in Fig. 1a and b for each LES case in Table 1. Increased surface cooling leads to stronger mean gradients in $\langle U \rangle_{\perp}$ and $\langle \theta \rangle$, an increased super-geostrophic maximum jet speed, and a reduction in the PBL depth. The trend most relevant to the present analysis is the behavior of the mean gradients near the surface and away from the influence of the jet. Accordingly, the bottom 25% of the PBL based on z_i is chosen as the region of interest. In the context of the turbulent kinetic energy (TKE) budget, there is an approximate local equilibrium between shear production, buoyancy damping, and dissipation of energy at each height within this region. This range includes heights above the surface layer, i.e., beyond $0.1h$, where the approach to z -less stratification is more evident.

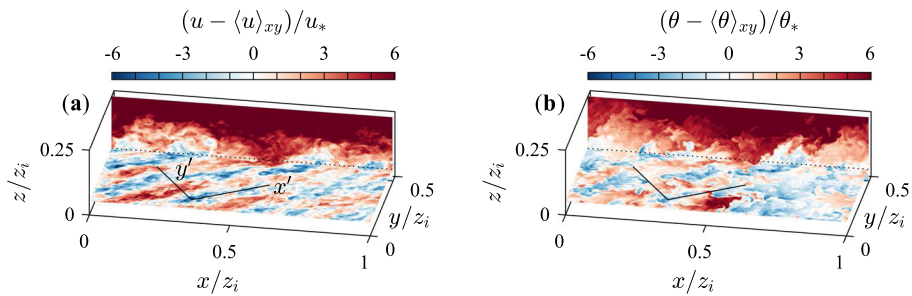


Fig. 2 Example regions of coherent momentum (a) and temperature (b) visualized along the x - y and x - z planes. The example is from the weakly stable case with $z_i/L = 1.7$. The x - y plane shown corresponds to $z = 0.05z_i$. The (x', y') notation refers to the horizontal coordinates oriented with the mean wind direction at the surface

The mean gradients are compared to the log law scaling parameters in Fig. 1c and d, where $\partial \langle U \rangle_{\perp} / \partial z = u_* / \kappa z$ is expected within the surface layer for neutral conditions, yielding a logarithmic dependence on z upon integration. As predicted by M-O similarity, the deviation from log law scaling increases with both height z and stratification L^{-1} . These deviations comprise a linear addition to the logarithmic profile for weak stratification in the original theory, and the mean dimensionless profiles asymptote to this linear (i.e., z -less) component for $z \gg L$ (Monin and Obukhov 1954). Figure 1e and f includes corrections to the gradients $\partial \langle U \rangle_{\perp} / \partial z = (u_* / \kappa z) \phi_m$ and $\partial \langle \theta \rangle / \partial z = (\theta_* / \kappa z) \phi_h$ based on common empirical similarity relations for momentum $\phi_m = (1 + 4.7z/L)$ and heat $\phi_h = (0.74 + 4.7z/L)$ (Businger et al. 1971). The similarity relations account for a large majority of the deviation from log law scaling of the mean profiles in the lowest 25% of the PBL. Yet, the residual differences are non-negligible and exhibit a possible stability trend, as evidenced by the inset panels of Fig. 1e and f. Also apparent from the inset panels is an approximate 10% deviation from the log law for the near-neutral case in the lowest 10% of the PBL. The difference is attributed in part to minor top-down buoyancy effects discussed previously that are not accounted for by the surface parameters and $L(z = 0)$. Note that the 10% difference is small compared to the stability effects seen for the other cases in Fig. 1c. While minor discrepancies are noted here, the primary focus for the remainder of the study is the large deviations from log law scaling and how these deviations are related to the underlying eddy organization. The following sections detail the detection of these eddies and assess the eddy properties in the context of the mean profiles.

2.2 Grid Orientation and Resolution Considerations

For neutral and weak stratification, the coherent velocity regions in the inertial layer organize as elongated streaks of low and high momentum (e.g., Hutchins and Marusic 2007; García-Villalba and del Álamo 2011). These streaks are apparent in the x - y horizontal plane of instantaneous flow realizations such as the example in Fig. 2a. Here, “ $\langle \cdot \rangle_{xy}$ ” indicates the spatial average at the height of the horizontal plane $z = 0.05z_i$. Similar features are present in Fig. 2b turbulent temperature field, but there is notably less coherence across longer distances such that the uniform temperature regions do not appear as “streaks”. There is significant overlap in the regions of negative and positive fluctuations in 2a and 2b which has been similarly observed for convective flows (Khanna and Brasseur 1998; Krug et al. 2020).

The coherent velocity and temperature regions cross through the $x-z$ vertical plane that is also shown in Fig. 2, leaving a visible signature in this plane. However, due to Coriolis effects, the near-surface turbulent features are not oriented with the geostrophic wind direction (x). To align the forthcoming analysis with the orientation of these features, the horizontal plane was rotated according to the mean wind direction in the lowest 10% of the PBL. The bulk average wind direction below $0.1z_i$ was used in each stability case such that the same rotation angle was employed for all heights in a given flow volume. The rotated coordinates (x', y') are indicated in Fig. 2 and are closely aligned with the velocity streaks. Compared to the original $x-y$ plane, the uniform velocity and temperature regions are apparent across larger distances along x' , which greatly facilitates the detection of the zones. The velocity component along x' , given the notation $u_{x'}$, is calculated by first rotating the horizontal velocity along the new (x', y') coordinate system at the original grid points, and then using two-dimensional linear interpolation to estimate the velocities at new grid points aligned with x' . The interpolation employed the same grid spacing Δ as the simulations and was conducted *a posteriori* on output flow volumes.

Figure 3 shows example instantaneous realizations of $u_{x'}$ and θ interpolated along the $x'-z$ plane, as well as the corresponding vertical gradients. The fields are normalized such that the velocity and temperature values range from 0 at the surface to 1 at z_i , with the notable exception of the super-geostrophic wind speed for the low-level jet. The organization of the instantaneous turbulence into relatively uniform zones is apparent for both quantities as indicated by similarity in color across large regions in the lower half of the PBL in Fig. 3a and c. The temperature field in Fig. 3c appears to be more well-mixed within the zones and exhibits more distinct temperature fronts visible from Fig. 3d. The thin shear layers are less striking in Fig. 3b, and the largest gradient values do not extend across the entire zone edge in every instance (Gul et al. 2020), but several high-shear regions are apparent in the lowest portion of the example field.

The LES resolution is likely a critical factor for the simulations to reproduce the observed uniform zones. Coarser resolution will yield a larger effective SGS viscosity such that the SGS dynamics along the gradient layers will be spread across wider distances, i.e., the gradient layers will appear less “thin”. If Δ is comparable to the expected zone size, the distinction between the zones and the gradient layers along their edges will be lost. The same is true for experiments at low Reynolds number, where sufficient scale separation between the inertia-dominated zones and the viscous shear layers is required for the UMZ organization to become apparent (see, e.g., de Silva et al. 2017). The grid resolution also influences the statistical detection of zones as discussed in the following section.

2.3 Uniform Momentum Zone Detection

Because the along-wind velocity component within a UMZ is relatively uniform by definition, the velocities at grid points within the zone tend to cluster around a single value representative of the UMZ. This tendency yields a statistical signature for the UMZs, where the grid points with similar velocity value manifest as a distinct peak in velocity histograms of instantaneous flow realizations (Adrian et al. 2000; de Silva et al. 2016). The automated detection of UMZs (and UTZs) from these histograms is sensitive to design parameters for both computing the histogram and identifying its peaks (de Silva et al. 2016; Laskari et al. 2018; Heisel et al. 2018). These sensitivities make it necessary to correctly fix the parameters for all flow cases within a given study, and make it challenging to conduct quantitative comparisons across different studies that employ varying detection parameters. The conclusions drawn here thus

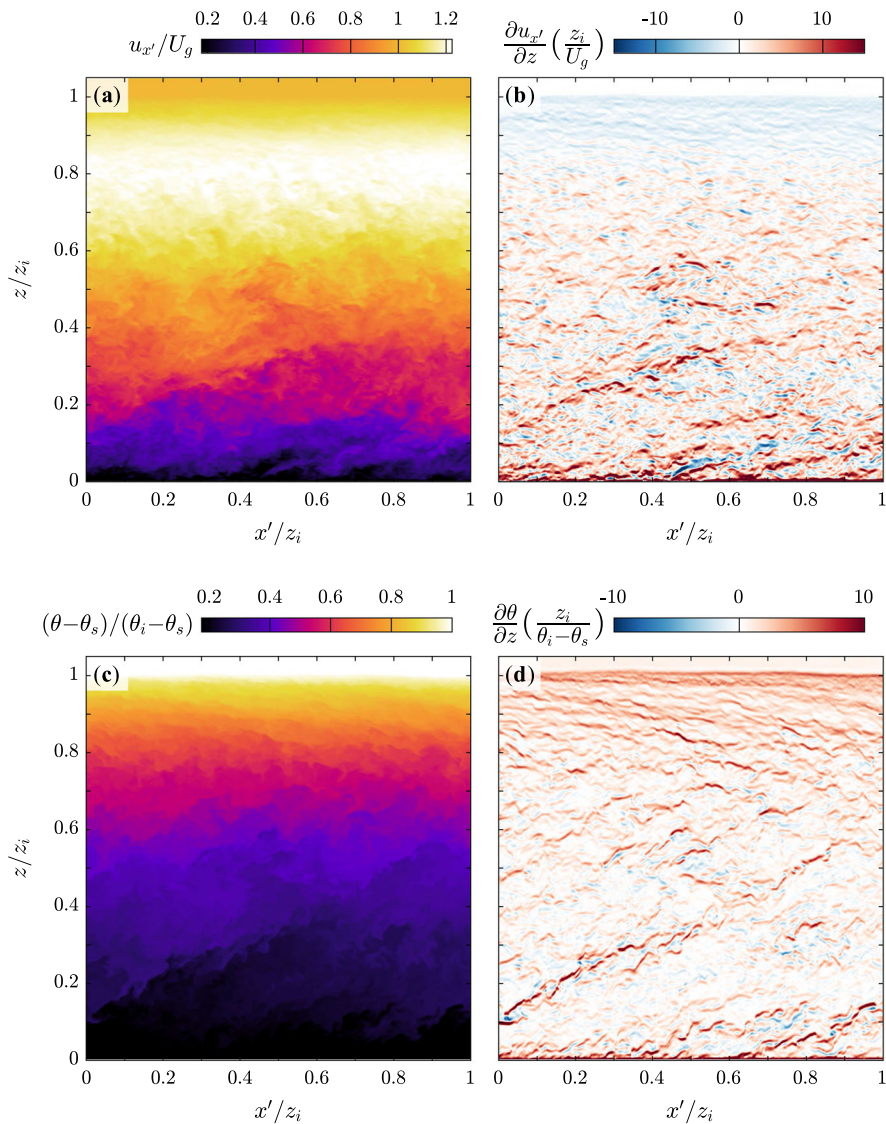


Fig. 3 Example velocity (a), velocity gradient (b), temperature (c), and temperature gradient (d) fields along the $x'-z$ plane oriented with the mean wind direction at the surface. The example is from the weakly stable case with $z_i/L = 1.7$. The values are normalized by the geostrophic wind speed U_g , mean surface temperature θ_s , and mean temperature θ_i at the inversion height z_i

focus on robust trends across the flow cases rather than exact quantitative properties of the detected zones.

The foremost design parameter is the size of the local flow volume used to compute each histogram, where the size is often expressed in terms of the along-wind distance $\mathcal{L}_{x'}$. The appropriate scaling for $\mathcal{L}_{x'}$ depends on the specific study, where the consequences for various scaling options are discussed elsewhere (de Silva et al. 2016; Heisel et al. 2018, 2020). If $\mathcal{L}_{x'}$ is large relative to the extent of UMZs near the surface, numerous UMZs and their velocity

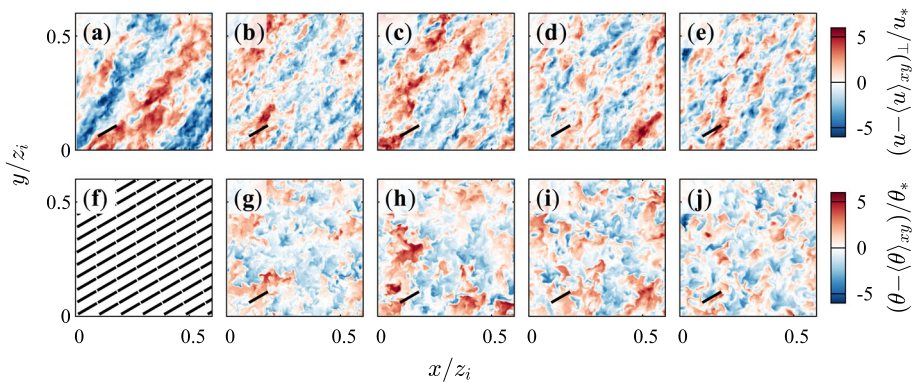


Fig. 4 Fluctuations of the horizontal velocity magnitude (top row) and temperature (bottom row) in the horizontal x – y plane at $z = 0.05z_i$. **a** $z_i/L = 0$; **b,g** $z_i/L = 1.7$; **c,h** $z_i/L = 2.4$; **d,i** $z_i/L = 3.2$; **e,j** $z_i/L = 6.0$. The black rectangle in each panel represents the size of a local area aligned with x' that is used for the zone detection. An array of local detection areas is provided for reference in **f** rather than the temperature fluctuations due to negligible θ_* in this case

clusters blend together such that the distinct histogram peaks are lost. In contrast, a small $\mathcal{L}_{x'}$ can yield spurious peaks due to measurement noise and resolution limitations (see, e.g., Figure 8 of Heisel et al. 2018). The distance $\mathcal{L}_{x'} = 0.1z_i$ employed here matches the value of a similar study that evaluated properties of UMZs in the inertial layer (Heisel et al. 2020). A sensitivity analysis demonstrated that increasing $\mathcal{L}_{x'}$ leads to the detection of fewer UMZs, but the agreement across flow cases does not change if $\mathcal{L}_{x'}/z_i$ is matched (Heisel et al. 2020). In other words, fixing $\mathcal{L}_{x'}$ relative to a fraction of the PBL depth ensures the effects of UMZ blending and histogram convergence are the same across each case in Table 1.

While UMZs are inherently three-dimensional regions within the flow, many previous studies have been limited to detection of UMZs along two-dimensional transects due to the use of planar measurement techniques such as particle image velocimetry (see, e.g., Meinhardt and Adrian 1995). Here, a three-dimensional local flow volume with finite thickness along y' is used to improve the statistical convergence of the histograms and the resulting UMZ signature. The extent of UMZs in the transverse direction (y') is not known *a priori* for the analysis. The distance $\mathcal{L}_{y'} = 0.01z_i$ used here for the width of the local flow volume is expected to be small relative to the width of the coherent regions. This width corresponds to five grid points. The horizontal area represented by $\mathcal{L}_{x'}$ and $\mathcal{L}_{y'}$ is shown in Fig. 4 in the context of near-surface turbulent fluctuations for each stability case. The horizontal area used for zone detection is smaller than or comparable to the coherent regions of velocity and temperature in each case. Hence, the choice of $\mathcal{L}_{x'}$ and $\mathcal{L}_{y'}$ is expected to manifest distinct histogram peaks for these regions. Trends in the apparent coherence at scales larger than the detection area are discussed later.

The number of grid points within each local flow volume is determined predominately by z_i due to the scaling of $\mathcal{L}_{x'}$ and $\mathcal{L}_{y'}$. To mitigate the influence of different resolutions on the statistical convergence of the histograms, the data volumes are resampled to a matched grid spacing $\Delta = 0.003z_i$ for each case. This value corresponds to the original resolution of the near-neutrally stratified LES, a 52% increase in Δ for the $z_i/L = 1.7$ case, and an 18% increase for $z_i/L = 6.0$. The final consideration for the local flow volume is its depth, which is limited here to the center of the low-level jet where the wind speed is maximized.

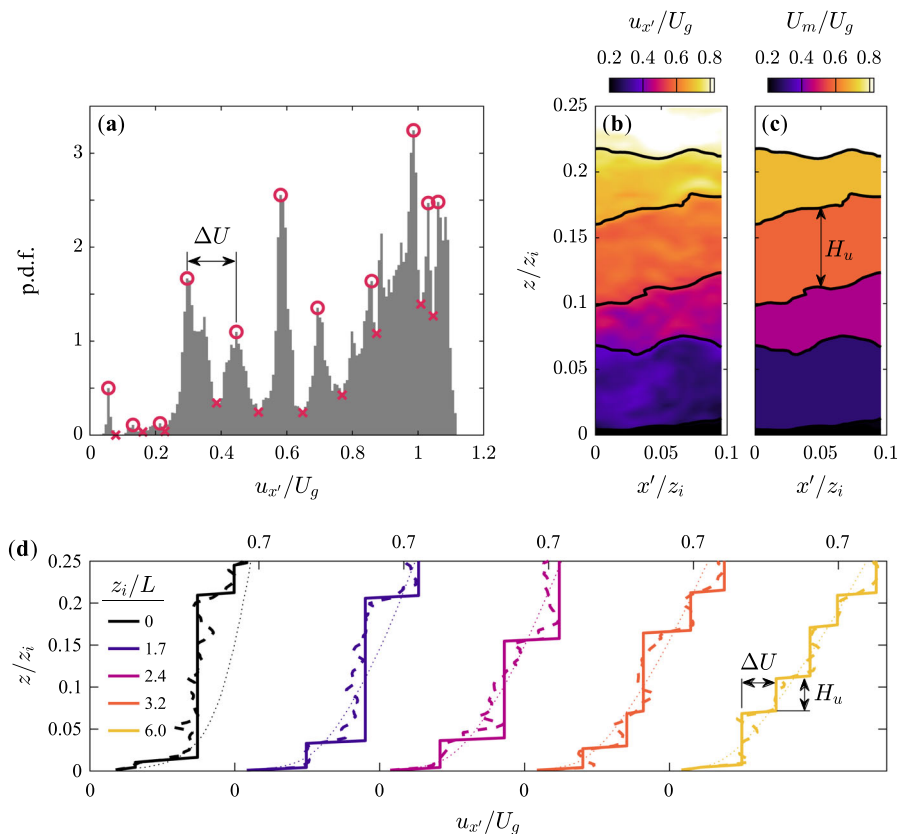


Fig. 5 Example detection of uniform momentum zones (UMZs). **a** Local histogram of the along-wind velocity component $u_{x'}$, where each peak (circles) corresponds to the modal velocity U_m of a quasi-uniform zone and the minima (crosses) correspond to the zone boundary. **b** Velocity field overlaid with isocontours of the velocity minima in **(a)** for the lowest 25% of the PBL. **c** The modal representation U_m of the same velocity field. **d** Example instantaneous vertical profiles for each stability case comparing an LES velocity $u_{x'}$ (dashed lines), its modal representation U_m (solid lines), and the ensemble average $\langle u_{x'} \rangle$ (dotted lines). The example in **(a,b,c)** is from the most stable case with $z_i/L = 6.0$

Figure 5a shows an example histogram computed using values of the resampled velocity $u_{x'}$ within a volume confined by $\mathcal{L}_{x'}$, $\mathcal{L}_{y'}$ and the jet height. The histogram is normalized as a probability density function (p.d.f.). An $x'-z$ plane from the same local flow volume is presented in Fig. 5b, where only the lowest 25% of the PBL is shown to emphasize the visual signature of UMZs in the region of interest. The UMZs in Fig. 5b correspond to the distinct peaks up to approximately $0.7U_g$ in Fig. 5a. The histogram peaks are noticeably less definitive for higher velocities associated with positions that are farther from the surface and above the range shown in Fig. 5b. This behavior is attributed in part to Coriolis effects and directional shear. The rotated velocity component $u_{x'}$ and narrow local flow volume become significantly misaligned with the mean wind direction far from the surface, which is another reason the later analysis is limited to the lowest portion of the PBL.

In addition to the definition of the local flow volume, the width of the discrete histogram bins affects the apparent statistical convergence and peaks resulting from the histogram. The

selected bin width $0.3u_*$ is similar to values employed in previous studies (Heisel et al. 2018, 2020). The bin width was chosen by evaluating how the number of detected histogram peaks changed as the width decreased and choosing a width after the number of peaks became relatively invariant. Repeating the entire analysis for an alternate bin scaling $0.01U_g$ (de Silva et al. 2016) did not change the conclusions of the study.

The next step in the UMZ detection is defining a peak. Threshold parameters are used to determine whether a local maximum in the histogram is detected as a peak or assumed to be spurious. The parameters include the minimum peak prominence that measures the height of the peak above the neighboring local minima (Laskari et al. 2018). Here, a given local maximum must be 15% greater than the adjacent local minima to be identified as a peak. In the Fig. 5a example, several maxima at $0.35U_g$ and above $0.8U_g$ are excluded due to this threshold. The area of the peak is calculated as the integral of the p.d.f. between the local minima adjacent to the peak. This area corresponds to the number of grid points associated with the UMZ and thus the size of the UMZ. A minimum threshold of 0.01 (i.e., 1% of both the p.d.f. and the local flow volume) is applied to the peak detection. The appropriate threshold parameters can vary between studies based on the data resolution and presence of measurement noise. The most important detail for the present study is the consistency of the local flow volume, resolution, and detection parameters across the cases considered.

The detected peaks resulting from the above parameters are indicated by circle markers in Fig. 5a. Each peak indicates the presence of a UMZ and its representative modal velocity U_m (de Silva et al. 2016). The thin shear layers along the UMZ edges span a relatively large range of $u_{x'}$ across a small distance, resulting in a limited number of grid points corresponding to the velocity along the shear layer. The representative velocity of the UMZ edges can therefore be defined using the local minima between detected peaks (Heisel et al. 2018), shown as “x” markers in Fig. 5a. The spatial position of the UMZ edges, e.g., the black lines in Fig. 5b, is estimated using isocontours of the representative edge velocity.

The turbulent field can be approximated as a series of UMZs by assuming perfect mixing $u_{x'} = U_m$ throughout the UMZ extent as shown in Fig. 5c. The instantaneous vertical profile of velocity corresponds to a single column of Fig. 5b and c. An example instantaneous profile for each flow case is provided in Fig. 5d. The organization of the turbulent field into UMZs and thin shear layers yields a staircase shape in the instantaneous profiles (de Silva et al. 2016), where the approximately constant rises correspond to UMZs and the steps occur across the thin shear layers. The instantaneous profile shape is distinct from the smooth mean (dotted lines), indicating the mean is only achieved through long-term averaging and variability in the position of the steps across space and time (de Silva et al. 2017; Heisel et al. 2020).

The approximation of the profiles as a series of instantaneous steps appears reasonably accurate for each stability case in Fig. 5d. A quantitative assessment of the approximation is provided later in Sect. 3.1. The first relevant property of the UMZ organization and the staircase profiles is the difference ΔU in modal velocity between adjacent UMZs defined as the difference between p.d.f. modes in Fig. 5a. The velocity ΔU is also the approximate “jump” in $u_{x'}$ across the thin shear layers in Fig. 5d. The second property is the thickness H_u of the UMZs calculated as the vertical distance between edges as seen in Fig. 5c and d. Both ΔU and H_u are compiled for each x' position across the length $\mathcal{L}_{x'}$ of the volume.

Figure 5 demonstrates the histogram-based detection of UMZs for a single local flow volume. The process is repeated for a new volume until the entire LES domain is analyzed for a given output instantaneous flow realization. The arrangement of local flow volumes is shown in Fig. 4f, where the spacing between volumes along y' is $0.05z_i$. A notable limitation of the detection methodology is that continuity of the zones and their edges is not guaranteed across adjacent local flow volumes (see, e.g., appendix A of Heisel et al. 2022). Accordingly,

while the vertical thickness of zones H_u is captured here, the horizontal extent of the zones in x' and y' cannot be evaluated in the present analysis. The only purpose for using numerous local detection volumes in the LES domain is to increase the number of realizations for the ensemble statistics. For the sake of reproducibility, sample MATLAB scripts for extracting the rotated local flow volumes, detecting uniform zones, and computing zone statistics are available from a repository link provided at the end of the article.

Zone statistics are not shown for the bottom 5% of the PBL in later results. The grid resolution becomes coarse relative to the vertical extent of the turbulent features in this region, leading to issues in the zone detection and in the relevance of the zonal approximation at these heights. Additional challenges for many LES schemes in this region include the dependence of the flow on the wall model within the first several grid points above the surface and the ability of the SGS model to produce accurate SGS stress values near the surface (Mason and Thomson 1992; Larsson et al. 2015; Bose and Park 2018). Many of the statistics deviate strongly below $0.05z_i$ and are not considered representative of physical trends in the turbulence.

2.4 Uniform Temperature Zone Detection

The detection of UTZs follows the same principles as Sect. 2.3. An account of similarities and differences between the UMZ and UTZ detection is given here.

The same local flow volume with horizontal area defined by $\mathcal{L}_{x'}$ and $\mathcal{L}_{y'}$, as visualized in Fig. 4, is used to compute histograms of the turbulent temperature field. The resolution $\Delta = 0.003z_i$ is also fixed across flow cases. Rather than limiting the depth of the local flow volume based on the low-level jet, the region up to z_i is included in calculations of the temperature histograms.

Figure 6a shows a histogram of θ for the same local flow volume as the UMZ example in Fig. 5. The bin width is $0.3\theta_*$, matching the surface scaling used for the velocity histogram bins. The histogram peaks and UTZs are detected using the same thresholds as before for the relative prominence (15%) and minimum area (0.01). The magnitude of the near-surface p.d.f. peaks is generally between 1 and 3 for both the velocity and temperature example histograms. As seen in Fig. 3, the temperature field is significantly more layered in the vicinity of the low-level jet, leading to a greater quantity of smaller histogram peaks away from the surface value.

As before, the representative temperature of each UTZ is the modal (peak) value θ_m , and the edges are detected using isocontours of the minima between histogram peaks. The UTZs and their edges in Fig. 6b and c overlap significantly with the UMZs in Fig. 5b and c, specifically the edges located near $z = 0.1z_i$ and $0.17z_i$. There are also differences, notably for the near-surface zones. The example is emblematic of the turbulent velocity and temperature structure being closely, but not perfectly related.

The approximation of UTZs throughout the bottom 25% of the PBL leads to the familiar stairstep-shaped instantaneous profiles in Fig. 6d, where the steps are associated with temperature fronts (Sullivan et al. 2016). No large-scale organization of turbulent temperature eddies is expected for the near-neutrally stratified flow, and UTZs are not detected for this case. The UTZ properties for the remaining cases are characterized in terms of the temperature difference $\Delta\theta$ between adjacent zones and the vertical thickness H_θ of the zones. Statistics for $\Delta\theta$ and H_θ are compiled for instances throughout the flow volume in the same manner as for the UMZs.

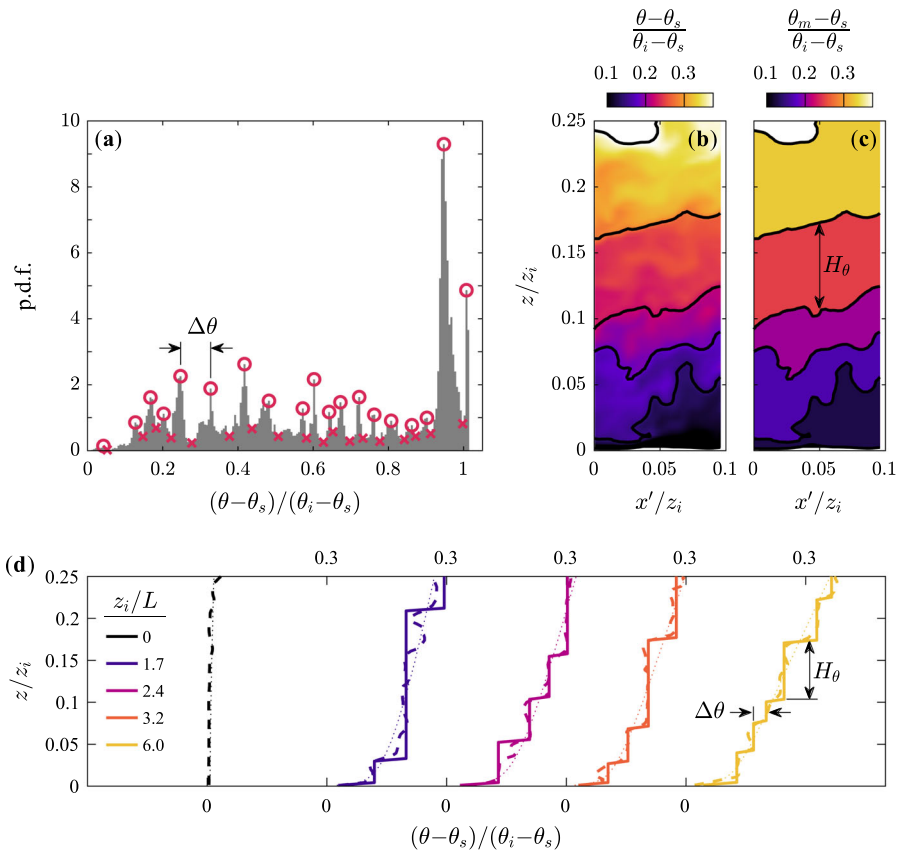


Fig. 6 Example detection of uniform temperature zones (UTZs) showing the same local flow field as Fig. 5. **a** Local histogram of temperature, where each peak (circles) corresponds to the modal temperature θ_m of a quasi-uniform zone and the minima (crosses) correspond to the zone boundary. **b** Temperature field overlaid with isocontours of the temperature minima in (a) for the lowest 25% of the PBL. **c** The modal representation θ_m of the same temperature field. **d** Example instantaneous vertical profiles for each stability case comparing an LES temperature θ (dashed lines), its modal representation θ_m (solid lines), and the ensemble average $\langle \theta \rangle$ (dotted lines)

2.5 Methodology Summary

The LES of the PBL (Sullivan et al. 2016) is based on the GABLS benchmark study (Beare et al. 2006). The LES includes five stability conditions ranging from near-neutral to almost z-less stratification to explore the parameter space of interest. The key scaling parameters for each case are listed in Table 1.

Figure 1 shows average profiles of the horizontal wind speed and temperature. Deviations in the profiles from the log law scaling parameters under increasing stratification are evident from the gradients in Fig. 1c and d. The focus of the study is how these deviations are related to properties of the instantaneous turbulence organization, and how these properties are accounted for in M-O similarity relations such as in Fig. 1e and f.

The near-surface coherent regions in the instantaneous turbulent flow, including elongated momentum streaks, are aligned with the surface wind direction that differs from the

geostrophic wind direction due to Coriolis effects. These near-surface features are visualized in Fig. 2. To align the analysis with these features, the horizontal plane of the LES output flow volumes is rotated according to the surface wind direction. The rotated coordinate system is given the notation (x', y') as seen in Fig. 2.

The coherent regions in Fig. 2 are also apparent in the $x'-z$ plane as seen in Fig. 3, where the vertical layering of the regions creates the appearance of uniform zones separated by thin edges with enhanced gradients. Each uniform zone creates a distinct peak in histograms of the local flow volume. The representative value of the zone is given by the peak mode, and the zone edges are indicated by the minima between peaks. Detected modes and minima for an example histogram are shown in Fig. 5a for UMZs and Fig. 6a for UTZs. The corresponding zones in the $x'-z$ plane are also shown in Figs. 5 and 6 for UMZs and UTZs, respectively, where the edge positions are estimated from isocontours of the detected minima.

Figures 5d and 6d show instantaneous profiles of the velocity and temperature, respectively, where the organization of uniform zones and thin gradient layers creates a staircase-like shape in the profiles. The rises and steps are well approximated by the detected uniform zones for each flow case, such that the UMZ and UTZ properties can be used to relate the instantaneous turbulent structure to the smooth mean profile that results from variability in the position of the “steps” across long averaging periods. The zone properties are characterized here as the velocity difference ΔU between adjacent UMZs, the vertical thickness H_u of UMZs, the temperature difference $\Delta \theta$ between adjacent UTZs, and the vertical thickness H_θ of UTZs.

Section 3 presents average statistics for these zone properties at heights between $0.05z_i$ and $0.25z_i$. At higher positions, the analysis is influenced by the behavior of the low-level jet and directional shear from Coriolis forces. Results are not shown for the bottom 5% of the PBL because limitations in the LES and uniform zone methodology bias the statistics at the lowest positions.

3 Results

3.1 Applicability of the Uniform Zone Approximation

The two foremost properties for the organization of UMZs and UTZs are the uniformity of the flow within each zone and the clustering of gradients along the zone edges. Both properties are quantitatively assessed here using the detected zones and edges. The goal is to determine whether the zonal organization of turbulent eddies is present for the stably stratified surface layer before proceeding to the evaluation of zone properties.

If small-scale statistics including vorticity, dissipation, and shear $\partial u_{x'}/\partial z$ are spatially intermittent and preferentially aligned with the UMZ edges, statistics for $\partial u_{x'}/\partial z$ computed at points along the edges will contribute disproportionately to the overall mean shear. The alignment can therefore be considered preferential if the contribution of the UMZ edges to $\partial \langle u_{x'} \rangle / \partial z$ is large relative to the fraction of the flow volume represented by the edges (de Silva et al. 2017). Figure 7a shows an example instantaneous flow field demonstrating the overlap between the high-shear regions and the detected UMZ edges.

The edge thickness must be known or assumed to determine which grid points are associated with each UMZ edge. As discussed in Sect. 2.2, the effective thickness is expected to depend on the resolution Δ and the eddy viscosity of the LES. A thickness $0.01z_i \approx 3\Delta$ is assumed here such that each edge spans three points on the interpolated grid. Note that

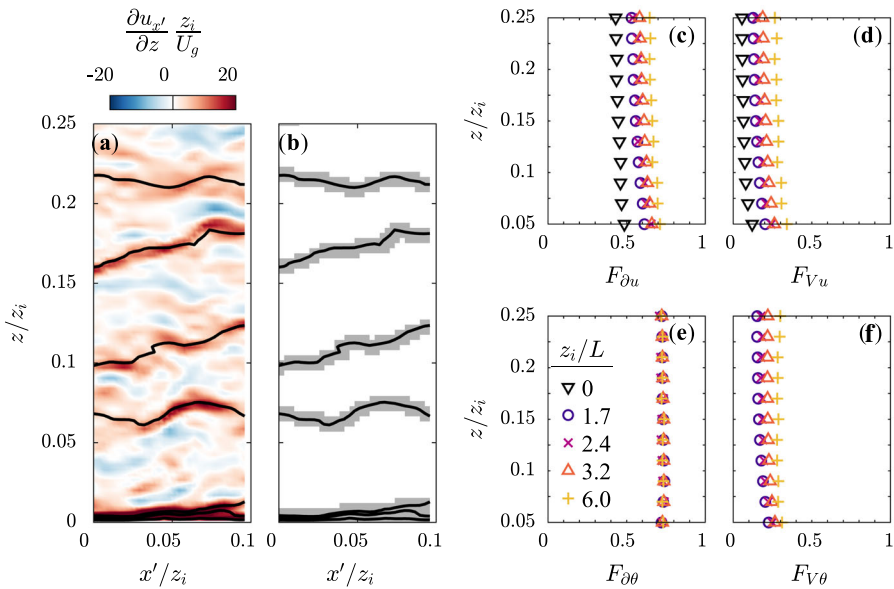


Fig. 7 Concentration of gradients along detected zone edges. **a** Velocity gradient $\partial u_{x'}/\partial z$ for the example field in Fig. 5b. **b** LES grid points along the zone edge, assuming the edge thickness is $0.01z_i$. **c** Fraction of the velocity gradient $F_{\partial u} = (\Sigma \partial u_{x'}/\partial z|_{edge})/(\Sigma \partial u_{x'}/\partial z)$ corresponding to the UMZ edges, computed in binned intervals of height z . **d** Fraction of the flow volume F_{Vu} corresponding to the UMZ edges. **e** Fraction of the temperature gradient $F_{\partial \theta} = (\Sigma \partial \theta/\partial z|_{edge})/(\Sigma \partial \theta/\partial z)$ corresponding to the UTZ edges. **f** Fraction of the flow volume $F_{V\theta}$ corresponding to the UTZ edges

moderately increasing or decreasing the assumed thickness does not change the conclusions drawn from the exercise. The points associated with the UMZ edges in Fig. 7a are identified in 7b for this assumed thickness.

The fractional contribution of these edge points to the shear statistics is $F_{\partial u} = (\Sigma \partial u_{x'}/\partial z|_{edge})/(\Sigma \partial u_{x'}/\partial z)$, where the numerator is the shear only for points along the edges and the denominator is equivalent to the mean gradient. The fraction is computed height-by-height to yield the profile shown in Fig. 7c. In each case, the instantaneous shear aligned with the UMZ edges accounts for 50–70% of the overall mean. The fraction of the volume F_{Vu} is estimated simply as the number of points along the edges divided by the total number of grid points at the given height. The volume fraction in Fig. 7d is less than 30% for each case. Results for the two fractions $F_{\partial u}$ and F_{Vu} confirm the clustering of instantaneous shear along the UMZ edges: the detected edges are a majority contributor to the mean shear despite occupying a small fraction of the flow volume. This trend continues beyond the plotted limits shown until $z/h \approx 2/3$, whereupon $F_{\partial u}$ and F_{Vu} both decrease significantly.

The same edge statistics are presented for the UTZs, namely the fractional contribution $F_{\partial \theta}$ to the temperature gradient in Fig. 7e and the fraction of the volume $F_{V\theta}$ in Fig. 7f. The volume fraction is approximately the same as for the UMZs, but the contribution to the mean temperature gradient exceeds 70%. The higher values for $F_{\partial \theta}$ are consistent with visual observations in Fig. 3 that the UTZ edges (i.e., temperature fronts) are more distinct than the UMZ edges.

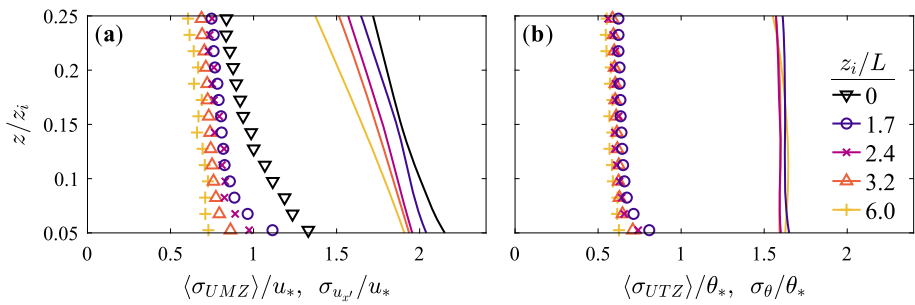


Fig. 8 Demonstration of zone uniformity using the root mean square (r.m.s.) of velocity and temperature within the detected zones. **a** The r.m.s. σ_{UMZ} of velocity within a UMZ, averaged across zones at a given height. **b** The r.m.s. σ_{UTZ} of temperature within a UTZ, averaged across zones at a given height. The zone r.m.s. statistics (symbols) are compared to the ensemble r.m.s. profiles $\sigma_{u_{x'}, \theta}$ (lines)

In the context of local dynamics along the zone edges, the gradient in the direction normal to the nearest detected edge is more relevant than the vertical component $\partial/\partial z$ presented here. For the grid points associated with the zone edges, the average temperature gradient normal to the edge is 15% greater than the vertical component for the weakly stable case, and the difference systematically reduces to approximately 10% for the most stable case. The decreasing trend is attributed to the reduction in structural inclination for the stable surface layer (Liu et al. 2017), i.e., the zone edges are closer to horizontal. While the derivative normal to the zone edge is greater, the vertical derivative is utilized for the statistics in Fig. 7 to better assess the contribution of the edge regions to the overall mean vertical gradients.

Previous studies have demonstrated the uniformity of detected UMZs by showing the variability within each zone to be relatively small (de Silva et al. 2016; Heisel et al. 2018). The variability is measured here as the root mean square (r.m.s.) of velocity values across all points within a detected UMZ, excluding the edge points visualized in Fig. 7b. The r.m.s. values are then averaged for all UMZs at a given position based on the UMZ midheight, resulting in the profiles $\langle \sigma_{UMZ} \rangle(z)$ shown in Fig. 8a. Variability within the UMZs is less than half of the overall r.m.s. of the LES velocity $\sigma_{u_{x'}}$ that is also included in Fig. 8a. The same variability statistics for UTZs are shown in Fig. 8b, where $\langle \sigma_{UMZ} \rangle$ is almost three times smaller than σ_θ .

The zone variability and LES r.m.s. are not directly comparable, because unlike for $\sigma_{u_{x'}, \theta}$, the r.m.s. within a single zone is computed across a range of heights spanned by that zone. Calculating the r.m.s. height-by-height within each zone yields an even greater reduction in the variability compared to $\sigma_{u_{x'}, \theta}$. The variance resulting statistically from the turbulent fluctuations is therefore predominately due to the passage of numerous uniform zones rather than the fluctuations within each zone (Heisel et al. 2018). The residual variability within the UMZs and UTZs is attributed to relatively weak space-filling fluctuations whose organization (or lack thereof) does not contribute directly to the mean flow statistics but is closely related to scale-dependent trends (Heisel et al. 2022).

The results suggest that turbulence in the lowest portion of the stably-stratified PBL is approximately organized as a series of uniform zones (Fig. 8) and thin layers aligned with the largest gradients (Fig. 7). The statistics support the visual evidence in Figs. 5d and 6d. Further, there is no indication that the organization weakens with increasing stratification, at least within the fully turbulent regime in the absence of global intermittency. The stability trend for the volume fraction in Fig. 7d and f is related to the zone thicknesses presented

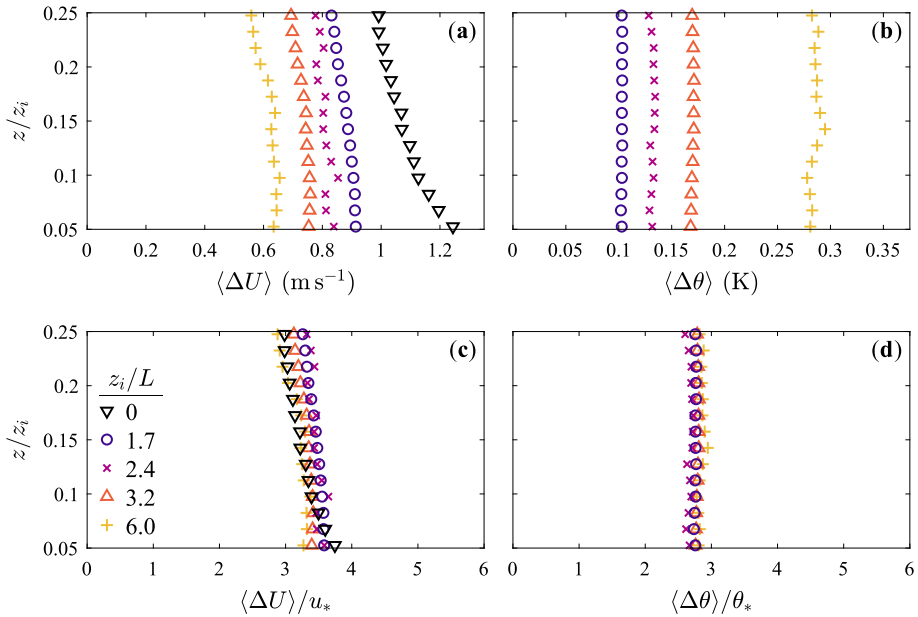


Fig. 9 Profiles of the mean difference in velocity and temperature between vertically adjacent zones. **a, c** Velocity difference between UMZs $\langle \Delta U \rangle$ as defined in Fig. 5. **b, d** Temperature difference between UTZs $\langle \Delta \theta \rangle$ as defined in Fig. 6. The profiles are shown dimensionally and relative to the surface scaling parameters

later. The smaller gradient contribution in Fig. 7c and larger variability in Fig. 8a for the near-neutral case may be related to the coarser native resolution Δ/z_i of the simulation and its effective eddy viscosity as previously discussed.

3.2 Zone Velocity and Temperature

The characteristic velocity ΔU and temperature $\Delta \theta$ of detected zones correspond to sharp changes or “jumps” in value across the gradient layers as seen in Figs. 5d and 6d. The compiled statistics for ΔU and $\Delta \theta$ are averaged here in binned intervals of height based on the position of the zone edge where the jump occurs. Profiles of the binned averages are shown in Fig. 9.

The profiles are shown dimensionally in Fig. 9a and b to demonstrate the clear stability trends, and are plotted relative to the surface parameters u_* and θ_* in Fig. 9c and d, respectively. The surface parameters yield agreement across all cases for both ΔU and $\Delta \theta$.

The result $\Delta U \sim u_*$ and the moderate decrease in $\Delta U(z)$ with height are both consistent with previous studies (de Silva et al. 2017; Heisel et al. 2020), including field measurements in the neutrally stratified surface layer (Heisel et al. 2018). In canonical turbulent boundary layers, the relation $\Delta U \sim u_*$ extends to the top of the boundary layer (Heisel et al. 2020). It is not known if ΔU is invariant with height in a true logarithmic region near to the surface. As discussed, the resolution becomes a limiting factor in the lowest portion of the boundary layer, both for the present LES and for the previous experimental measurements referenced above. The UMZ detection and ΔU calculations were repeated using the magnitude of the horizontal velocity rather than the rotated component $u_{x'}$. The velocity ΔU was modestly

larger in this case, but the same height dependence and agreement across cases for $\Delta U/u_*$ were observed. The directional shear therefore does not change the primary trends in ΔU below $0.25z_i$.

In contrast to the velocity, the temperature $\Delta\theta$ is approximately constant with height in Fig. 9d. The magnitude of the difference relative to the surface parameters is moderately smaller for $\Delta\theta$ than ΔU . Considering the same bin width (i.e., $0.3u_*$ and $0.3\theta_*$) was employed in the zone detection, the differing intensity may be a physical characteristic of the turbulence. The trend is further discussed in Sect. 3.5.

The results in Fig. 9c and d indicate that the characteristic intensities ΔU and $\Delta\theta$ of the persistent eddy organization maintain a close proportional dependence on the surface fluxes regardless of the stratification, where the surface properties u_* and θ_* are the relevant scaling parameters for the logarithmic profiles $\partial U/\partial z = u_*/\kappa z$ and $\partial\theta/\partial z = \theta_*/\kappa z$. The result is unsurprising considering the absence of alternate velocity scales such as w_* that become relevant for convective conditions. For stable stratification, the turbulence is shear-driven such that the turbulent variance and kinetic energy are produced solely by a shear production mechanism characterized by u_* . Likewise, production of temperature variance is directly related to θ_* .

3.3 Zone Thickness

Given the agreement of ΔU and $\Delta\theta$ with the respective log law parameters u_* and θ_* in Fig. 9, deviations from the logarithmic profiles must predominately correspond to changes in the geometry of the uniform zones. The geometry is characterized in terms of the vertical zone thickness H_u and H_θ as shown in Figs. 5d and 6d. The compiled thickness statistics are averaged here in binned intervals of z , where the representative position of each zone is taken to be its midheight. Profiles of the average zone thickness are shown in Fig. 10.

The dimensional profiles in Fig. 10a and b reveal the expected trends in both height and stability. For near-neutral stratification, the UMZ thickness appears to increase proportionally with height z , matching previous experimental observations (Heisel et al. 2020). The presence of weak stability leads to a sharp reduction in the zone thickness, consistent with the pancake-like structure observed for stratified turbulence (e.g., Caulfield 2021). In the $z_i/L = 1.7$ case, a height dependence is still observed for both H_u and H_θ , but the zones are several times thinner than for near-neutral conditions.

The reduction in H_u and H_θ continues with increasing stratification. The smaller zones lead to more numerous “steps” and a stronger mean gradient in Fig. 5d and 6d. The increased number of steps also leads to the zone edges representing a larger fraction of the flow as seen in Fig. 7d and f. For $z_i/L = 6$ in Fig. 10a and b, the thickness appears invariant with height relative to the near-neutral case, particularly for heights above $0.1z_i$. The observed eddy geometry therefore spans the range from “attached” in accordance with log law predictions for the near-neutral PBL to relatively independent of height in accordance with the regime of z -less stratification.

For each LES case, an approximate local equilibrium between shear production, buoyancy damping, and dissipation is observed within the lowest 25% of the PBL that is the target region of the study. The equilibrium can be used to account for the UMZ thickness trends in Fig. 10a. Under these equilibrium conditions, i.e., for steady state flow with negligible transport by turbulence and pressure (Wyngaard 1992), the TKE budget is

$$0 = -\langle u'w' \rangle \frac{\partial \langle U \rangle}{\partial z} + \frac{g}{\langle \theta \rangle} \langle w'\theta' \rangle - \epsilon; \quad (1)$$

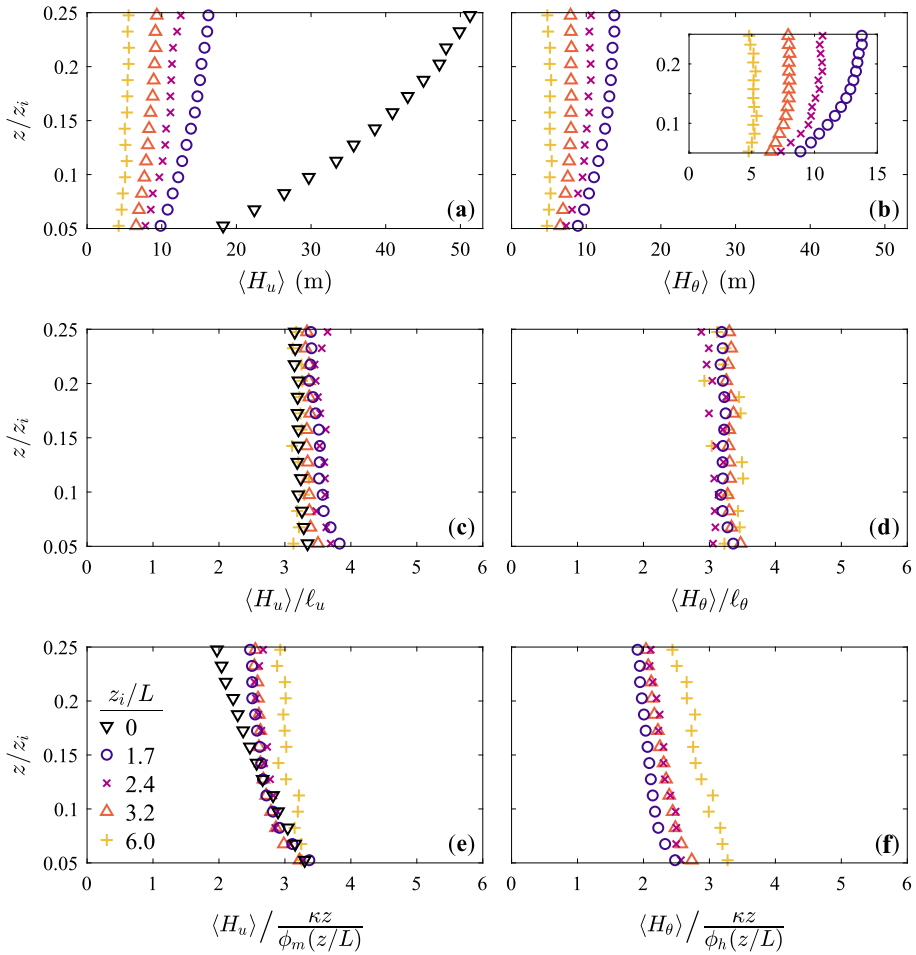


Fig. 10 Profiles of the mean zone thickness. UMZ thickness $\langle H_u \rangle$ as defined in Fig. 5, shown dimensionally (a), relative to the length ℓ_u in Eq. 3 (c), and relative to the similarity relation for momentum ϕ_m (e). UTZ thickness $\langle H_\theta \rangle$ as defined in Fig. 6, shown dimensionally (b), relative to the length ℓ_θ in Eq. 5 (d), and relative to the similarity relation for heat ϕ_h (f)

where the right-hand side terms, respectively, represent shear production of turbulence, production or suppression of turbulence by buoyancy, and the rate of dissipation ϵ by viscosity. The observed spatial organization of eddies and the corresponding stairstep-like instantaneous profiles support the approximation of the average gradients using the local zone properties (Heisel et al. 2020):

$$\frac{\partial \langle U \rangle}{\partial z} \approx \frac{\langle \Delta U \rangle}{\langle H_u \rangle} \sim \frac{u_*}{\ell_u} \quad \text{and} \quad \frac{\partial \langle \theta \rangle}{\partial z} \approx \frac{\langle \Delta \theta \rangle}{\langle H_\theta \rangle} \sim \frac{\theta_*}{\ell_\theta}. \quad (2)$$

Here, $\Delta U \sim u_*$ and $\Delta \theta \sim \theta_*$ are supported by Fig. 9, and the lengths ℓ_u and ℓ_θ are the parameters to be determined. Substituting for $\partial \langle U \rangle / \partial z \sim u_* / \ell_u$ in Eq. 1 and solving for ℓ_u yields the length scale

$$\ell_u = u_* \left(\frac{g \langle w' \theta' \rangle}{\langle \theta \rangle \langle u' w' \rangle} - \frac{\epsilon}{\langle u' w' \rangle} \right)^{-1} : \quad (3)$$

Note that Eq. 3 is specific to neutral and stable conditions because the zonal organization and the relations in Eq. 2 have not been evaluated for the convective PBL.

Figure 10c shows H_u relative to ℓ_u , where the dissipation term in ℓ_u is estimated using the model $\epsilon \approx C_\epsilon e^{3/2}/\Delta$ based on the SGS TKE e and constant $C_\epsilon = 0.93$ (Moeng and Wyngaard 1988; Sullivan et al. 2016). The agreement across cases and invariance with height validate the equilibrium assumed in Eq. 1 and confirm the connection between the gradient and zone properties in Eq. 2. Further, the use of local fluxes in the definition of ℓ_u is consistent with the concept of local scaling for stable conditions (Nieuwstadt 1984).

For the simplified budget in Eq. 1, the relative contributions of the dissipation ϵ and buoyancy $B = \frac{g}{\langle \theta \rangle} \langle w' \theta' \rangle$ to ℓ_u are related directly to the flux Richardson number R_f as $\epsilon/B = R_f^{-1} - 1$. Considering the flux Richardson number has a critical maximum value $R_f \approx 0.2$ under stable stratification (Yamada 1975; Grachev et al. 2013; Bou-Zeid et al. 2018), the buoyancy term is always at least four times smaller than the dissipation. The relatively small buoyancy contribution suggests that the approach to z-less stratification is predominately due to a reduced dependence on z in both $\partial U/\partial z$ and ϵ rather than the direct contribution of buoyancy in Eq. 1. The primary effect of the buoyancy term in Eq. 3 is a bulk reduction in ℓ_u that is proportional to θ_*/u_* .

The same equilibrium assumption can be used to infer a length scale ℓ_θ from the budget equation for temperature variance. The simplified budget for half the temperature variance is (Stull 1988; Mironov and Sullivan 2016)

$$0 = -\frac{1}{2} \langle w' \theta' \rangle \frac{\partial \langle \theta \rangle}{\partial z} - \epsilon_\theta : \quad (4)$$

where ϵ_θ is the molecular dissipation rate for temperature. Substituting for $\partial \langle \theta \rangle / \partial z \sim \theta_*/\ell_\theta$ from Eq. 2 in Eq. 4 and solving for ℓ_θ yields

$$\ell_\theta = -\frac{\theta_* \langle w' \theta' \rangle}{2\epsilon_\theta} : \quad (5)$$

The dissipation ϵ_θ is estimated here as $\epsilon_\theta \approx C_\theta e^{1/2} \theta_{sgs}^2 / \Delta$ using the constant $C_\theta \approx 2.1$ (Moeng and Wyngaard 1988). For this analysis, the variance of the SGS temperature θ_{sgs}^2 is approximated from the integral of the turbulent temperature spectrum extrapolated to infinite wavenumber.

Figure 10d shows H_θ relative to ℓ_θ . The ratio H_θ/ℓ_θ exhibits the same magnitude and agreement across cases seen for H_u/ℓ_u . The temperature variance budget contains no coupled term akin to the buoyancy damping in the TKE, such that the reduction in height dependence of H_θ and ℓ_θ with increasing stratification corresponds solely to trends in $\epsilon_\theta(z)$.

While ℓ_u and ℓ_θ more accurately captures the zone thickness trends when defined using local fluxes, it is informative to apply the surface scaling assumptions $\langle u' w' \rangle = -u_*^2$ and $\langle w' \theta' \rangle = -u_* \theta_*$. Substituting for surface parameters in Eq. 3 and multiplying the numerator and denominator by κz yields

$$\ell_u \approx \kappa z \left(\frac{z}{L} + \frac{\kappa z}{L_\epsilon} \right)^{-1} : \quad (6)$$

The length $L_\epsilon = u_*^3/\epsilon$ corresponds to the production range of scales in boundary layer flows (Davidson and Krogstad 2014; Chamecki et al. 2017; Ghannam et al. 2018), and simplifies

to $L_\epsilon \approx \kappa z$ in neutrally stratified conditions when dissipation and shear production are both approximately $u_*^3/\kappa z$.

The definition of ℓ_u in Eq. 6 is similar in form to existing mixing length models (e.g. Blackadar 1962; Delage 1974; Huang et al. 2013). Additionally, the denominator can be interpreted to represent departure from the log law scaling predicted by ϕ_m . As discussed previously, the loss of height dependence in ℓ_u predominately relates to $\kappa z/L_\epsilon$ diverging from unity, and is only modestly affected by the direct contribution of z/L . However, in traditional M-O relations the dissipative term $\kappa z/L_\epsilon$ is also parameterized in terms of z/L as $\kappa z/L_\epsilon = \epsilon \kappa z/u_*^3 = \phi_\epsilon(z/L)$. The relation $\phi_m = \phi_\epsilon + z/L$ (Hartogensis and de Bruin 2005) results naturally from Eq. 6 and is consistent with $\kappa z/L_\epsilon$ representing a majority of the similarity correction that is captured by ϕ_m .

The connection between ϕ_m and the UMZ geometry (through ℓ_u) is evaluated in Fig. 10e. The plot should match H_u/ℓ_u in Fig. 10c if the surface scaling assumption is accurate and if $(z/L + \kappa z/L_\epsilon) \approx \phi_m = (1 + 4.7z/L)$. The same comparison for the UTZ thickness is shown in Fig. 10f using $\phi_h = (0.74 + 4.7z/L)$. In both cases, the M-O relations account for a majority of the trends in height and stability of zone thickness that are observed in Fig. 10a and b. However, there is a notable difference in the $z_i/L = 6$ case and a moderate height-dependence that is likely related to the surface scaling assumption. These same discrepancies were noted previously for the mean gradients in Fig. 1e and 1f: ϕ_m and ϕ_h accurately describe the bulk of the deviation from the log law in the mean gradient profiles for each stability case, but also exhibit residual differences with a possible stability trend.

The purpose of the lengths ℓ_u and ℓ_θ is to explore the inter-related nature of the eddy organization, the turbulence budget contributions, and M-O similarity relations. The contribution of turbulent transport is neglected here, but is relevant to measurements in the roughness layer and around complex terrain (Heisel et al. 2020; Chamecki et al. 2020). The practical utility of the lengths is also limited by challenges in estimating ϵ and ϵ_θ . Further, the inclusion of dissipation in the definitions for ℓ_u and ℓ_θ should not be interpreted as causality, e.g., $\ell_u = f(\epsilon, \dots)$. Rather, it is expected that the properties of the integral-scale turbulence (e.g. ℓ_u and ℓ_θ) determine the required dissipation rate of the small scales in accordance with cascade theory (e.g., Pope 2000).

3.4 Zone Edge Layers

The previous statistics demonstrated the relevance of the surface parameters u_* and θ_* and length scales ℓ_u and ℓ_θ to the bulk properties of the uniform zone organization of turbulent eddies. These properties are related to the stairsteps of the instantaneous profiles in Figs. 5d and 6d. The zone scaling parameters and the stairstep pattern are also evident from the conditional average flow behavior around a zone edge, as demonstrated here.

Each detected zone edge has a position (x_e, z_e) corresponding to an isocontour of the representative edge velocity u_e or temperature θ_e . The representative value for each isocontour is determined from the p.d.f. minima as discussed in Sects. 2.3 and 2.4. Figure 11a shows the zone edges (black lines) for an example field. The flow profile around a zone edge can be computed in a frame of reference relative to the edge properties, e.g. velocity $(u - u_e)$ as a function of distance from the edge center $(z - z_e)$ as shown in Fig. 11b. Profiles of velocity $(u - u_e)$ and temperature $(\theta - \theta_e)$ were compiled in this reference frame for every edge position, and the profiles were averaged across edges with position $z_e \approx 0.1z_i$. The same methodology for computing conditional edge profiles has been applied to experimental measurements (de Silva et al. 2017; Heisel et al. 2021).

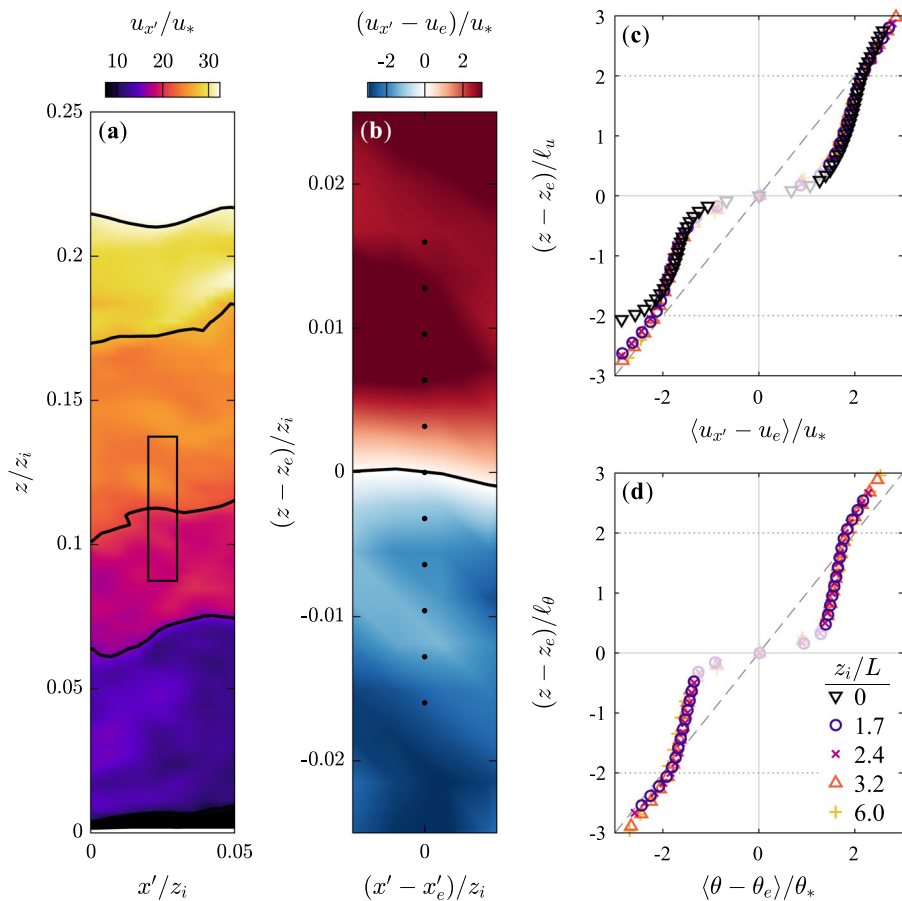


Fig. 11 Average profiles conditional to detected zone edges. **a** Example velocity field from Fig. 5b. **b** Velocity in the vicinity of a detected UMZ edge, i.e., the boxed area in **a**, relative to the edge position z_e and velocity u_e . **c** Velocity profiles relative to the detected edge. **d** Temperature profiles relative to the detected edge. The profiles are averaged across all edges at $z_e \approx 0.1z_i$, excluding instances where the nearest adjacent edge is within $2\ell_{u,\theta}$, i.e., the dotted lines in **c** and **d**. The dashed line represents the average gradient at z_e . Local dynamics within the edge layers (shown as transparent markers) are expected to depend strongly on the subgrid-scale model of the simulations

Figures 11c and d show the resulting averaged flow profiles centered around the detected zone edges. The collapse of the profiles provide further support for using u_* , θ_* , ℓ_u , and ℓ_θ to characterize the layered organization of turbulence in the stratified PBL. The zone edges and statistics represented by Fig. 11 were detected from a reanalysis with alternate histogram bin widths $0.01U_g$ and $0.005(\theta_i - \theta_s)$. The profiles suggest the scaling of the zone properties with u_* , θ_* , ℓ_u , and ℓ_θ observed in previous figures is not an artifact of the original bin widths. A notable exception in the collapse is the lowest z positions for the near-neutral case in Fig. 11c. The length ℓ_u varies strongly with z in this case, such that the value $\ell_u(z_e)$ at the center of the reference frame is not applicable to statistics far from the center.

The transparent markers in Fig. 11 represent the region in the immediate vicinity of z_e where the dynamics depend strongly on the SGS model and grid resolution. For turbulent

boundary layers, the thickness of the shear layers is proportional to the Taylor microscale (Eisma et al. 2015; de Silva et al. 2017; Heisel et al. 2021). The microscale depends on viscous processes that are not explicitly included in the present simulations. A majority of the jump in velocity and temperature occurs across this thin region, which is consistent with the preferential alignment of gradients in Fig. 7 and the jumps appearing as an approximate discontinuity in the instantaneous profiles.

The averages in Fig. 11c and d exclude instances in which the nearest adjacent edge is closer than $2\ell_u$ or $2\ell_\theta$, such that no other zone edges occur within the region bounded by horizontal dotted lines. The heights within these limits and away from the center $z = z_e$ therefore represent the interior of the uniform zones. As expected, the velocity and temperature vary weakly within this region relative to the sharp change at $z = z_e$. The mean gradients from Eq. 2 are included as dashed lines in Fig. 11. The individual components of the organized structure, i.e., the uniform zones and their edges, both have shapes differing significantly from the mean gradient, but the combined properties of the average edge and adjacent zone(s) matches the mean gradient across the extent of the zone from $(z - z_e) = 0$ to $2\ell_u$ and $2\ell_\theta$.

Outside the dotted lines, the profiles approximately match the mean gradient. Neighboring zone edges can appear at any height within this region. The alignment with the mean gradient in this region is due to variability in the position of these neighboring edges across different instantaneous profiles that contribute to the average. This is in contrast to the staircase shape within the dotted lines achieved by fixing the edge position in the average. The different behavior emphasizes the fact that the scaling behavior of the mean gradient corresponds closely to the existence and properties of the uniform zones, and the absence of the staircase signature in the mean gradient profile results from variability in the height of the zone edges across space and time.

3.5 Uniform Zones and the Turbulent Prandtl Number

The analysis thus far has demonstrated the contribution of the size and intensity of the prevailing turbulent eddies to the mean gradients. The approximation of the gradient based on the size (i.e., H_u and H_θ) and intensity (i.e., ΔU and $\Delta\theta$) is given in Eq. 2. The same principle can be applied to investigate the relation between the eddy organization and the turbulent Prandtl number:

$$Pr_t = \frac{\langle u'w' \rangle_\perp \frac{\partial \langle \theta \rangle}{\partial z}}{\langle w'\theta' \rangle \frac{\partial \langle U \rangle_\perp}{\partial z}} \approx \frac{\langle \Delta\theta \rangle / \langle w'\theta' \rangle}{\langle \Delta U \rangle / \langle u'w' \rangle_\perp} \frac{\langle H_u \rangle}{\langle H_\theta \rangle}. \quad (7)$$

The turbulent Prandtl number represents dissimilarity in the turbulent diffusivity of heat and momentum, and is a key parameter in modeling turbulence effects in the atmosphere (Kays 1994; Li 2019). Equation 7 implies that Pr_t depends on similarity in both the eddy intensity relative to the fluxes and in the eddy geometry. The components of Eq. 7 are shown in Fig. 12.

The comparison of the average differences ΔU and $\Delta\theta$ in Fig. 12a reveals that ΔU is consistently larger than $\Delta\theta$ relative to the fluxes for momentum and heat. The same trend is apparent from the differing magnitudes in Fig. 9c and d. The height dependence of ΔU observed previously in Fig. 9c is significantly weaker in Fig. 12a. The weaker trend in Fig. 12a is due to ΔU having a similar height dependence as the ratio of the local flux profiles $\langle w'\theta' \rangle / \langle u'w' \rangle_\perp$, where the momentum flux decays faster in height than the approximately linear heat flux profile for stable conditions (Nieuwstadt 1984). It is not clear from the present

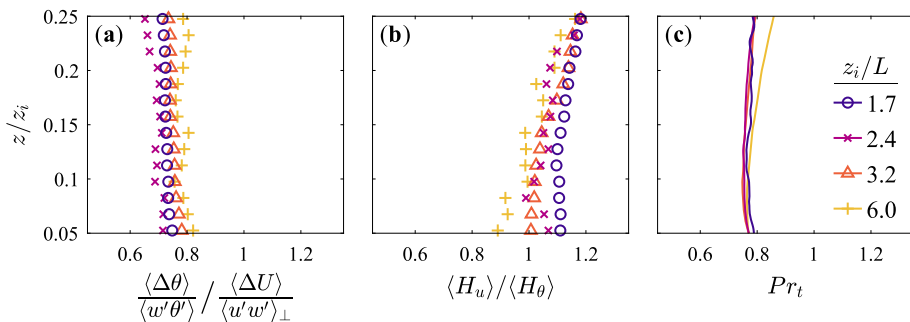


Fig. 12 Profiles illustrating the contribution of zone properties, i.e., eddy intensity and geometry, to trends in the turbulent Prandtl number. **a** Ratio of average differences $\Delta\theta$ and ΔU from Fig. 9, normalized by the local fluxes. **b** Ratio of average thicknesses H_u and H_{θ} from Fig. 10. **c** Turbulent Prandtl number $Pr_t = (-\langle u'w' \rangle_{\perp} \partial \langle \theta \rangle / \partial z) / (-\langle w'\theta' \rangle \partial \langle U \rangle / \partial z)$ corresponding to the product of **a** and **b**

results whether there is a phenomenological connection between the height dependence of ΔU and the deviation from linear decay in the momentum flux profile.

The ratio of zone thicknesses H_u/H_{θ} in Fig. 12b indicates the UMZs and UTZs have similar thickness in the surface layer below $0.1z_i$. The similar thicknesses are seen also in a comparison of Fig. 10a and b. The similarity is specific to the vertical extent of the zones, as the example fields in Fig. 4 indicate a level of dissimilarity in the horizontal extent. The thickness ratio deviates from unity away from the surface in Fig. 12b due to a weaker height dependence in the UTZ size that is also apparent in Fig. 10b. The increase in H_u/H_{θ} becomes more pronounced at higher positions above the plotted limits. The trend is related to the previous observation from Fig. 3 that the temperature field has more zones or “layers” compared to the velocity field in the upper portion of the PBL approaching the low-level jet.

As seen from Eq. 7, the Prandtl number in Fig. 12c results from the product of the ratios in panels a and b. The smaller diffusivity for heat, indicated by $Pr_t < 1$, can therefore be attributed to a weaker eddy intensity relative to the fluxes and surface parameters; the difference in temperature $\Delta\theta/\theta_*$ across the fronts is approximately 20% smaller than $\Delta U/u_*$ across the shear layers. The Prandtl number is approximately constant near the surface where the vertical extent of the uniform zones is similar. However, Pr_t increases with height above the limits of Fig. 12 where the UTZs become thinner and more numerous compared to the UMZs.

The trends in Fig. 12 also correspond to ϕ through the relation $Pr_t = \phi_m/\phi_h$. The M-O similarity relations used here follow a linear form $\phi = a + b(z/L)$. The difference in a for momentum ($a = 1$) and heat ($a = 0.74$) represents a shift in the gradient profiles that correspond directly to the discrepancy between $\Delta\theta/\theta_*$ and $\Delta U/u_*$. The relation between zone properties in Fig. 12a and b does not vary with height below $z \approx 0.1z_i$, which corresponds to the similarity in b for momentum and heat ($b = 4.7$ for both) and the approximately constant Pr_t within the surface layer.

4 Concluding Remarks

4.1 Overview

As computational and experimental capabilities have advanced in recent decades, there is a growing body of evidence that small-scale intermittency (i.e., non-uniform distribution of

dissipation in space and time) manifests as thin regions of intense small-scale features in instantaneous realizations of high-Reynolds-number turbulence (Ishihara et al. 2009; Hunt et al. 2010). This spatial intermittency results in visually striking patterns when the forcing conditions induce a preferential orientation in the clusters of small-scale eddies. For instance, the anisotropy for both boundary layer flows and stratified flows leads to distinct layers of elongated uniform regions separated by much thinner regions with intense gradients (Meinhart and Adrian 1995; Caulfield 2021). In the boundary layer case, the thin gradient regions have a positive average inclination relative to the horizontal plane as seen in Fig. 3, leading to the signature of ramp-like structures in two-point correlation statistics (Hutchins et al. 2012; Chauhan et al. 2013; Liu et al. 2017).

It is perhaps unsurprising that the same layered features are observed here for the stable PBL which is both wall-bounded and stratified. The layers in each realization are detected as UMZs and UTZs, which assumes the flow within the zones is uniform and that all gradients coincide with the zone edges. The assumption is supported by conditional statistics showing the gradients are preferentially aligned with the detected zone edges (Fig. 7) and the variability within the zones is small (Fig. 8). This persistent organization produces a staircase-shaped signature in instantaneous profiles that is well described by UMZs and UTZs as seen in Figs. 5d and 6d. The uniform zones can therefore be used to quantify the properties of the turbulent eddy organization and relate these properties to mean statistics that result from an ensemble of the instantaneous events.

For instance, the average differences ΔU and $\Delta \theta$ represent the sharp change in velocity and temperature, respectively, across the thin gradient layers associated with the zone edges. Both ΔU and $\Delta \theta$ remain proportional to the respective surface flux parameters u_* and θ_* for the range of stability simulated (Fig. 9). The vertical thicknesses H_u and H_θ of the UMZs and UTZs represents either the size of the well-mixed regions or the spacing between the gradient layers. The thickness is proportional to z for the near-neutral case, consistent with previous experimental observations (Heisel et al. 2020). The zones become progressively thinner and lose their height dependence as the stability regime approaches z -less stratification (Fig. 10). The scaling behavior in the zone properties indicate that departure from the log law mean profiles are almost entirely due to changes in the eddy size, such that the primary purpose of the M-O similarity relations ϕ_m and ϕ_h is to account for the reduced zone thickness (Fig. 10e and f). While the UMZs and UTZs have similar thickness in the surface layer below $0.1z_i$, i.e., $H_u \approx H_\theta$, the relative eddy intensity $\Delta \theta / \theta_*$ is approximately 20% smaller than $\Delta U / u_*$, leading to a turbulent Prandtl number below 1 (Fig. 12).

4.2 Limitations

Many aspects of the complex turbulent field are lost when the flow is simplified to a series of UMZs and UTZs. Dynamics and mixing cannot be directly explained by this framework due to the absence of rotation and the vertical velocity component in the zone definition. Further, the generic definition of the uniform zones does not capture the rich detail of momentum streaks (Dennis and Nickels 2011), roller modes (Jiménez 2018), hairpin vortices (Adrian et al. 2000), and temperature fronts (Sullivan et al. 2016), among other features. The analysis is therefore limited to the bulk properties that emerge from the arrangement of zones rather than more detailed, three-dimensional aspects of the zone and edge topology.

No conclusions can be made regarding the precise magnitudes for either the differences $\Delta U / u_*$ and $\Delta \theta / \theta_*$ in Fig. 9 or the thicknesses H_u / ℓ_u and H_θ / ℓ_θ in Fig. 10. These magnitudes depend on numerous variables discussed in Sect. 2.3 including the grid resolution, the

extent of the local flow volume, the histogram bin width, and the peak detection parameters. Changing these variables leads to fewer or more numerous detected histogram peaks and corresponding changes in the average zone properties. It was found that the changes are proportional across cases if the parameters are consistent, such that the trends in stratification or between velocity and temperature are robust even if the magnitudes are sensitive to the methodology.

4.3 Future Research Directions

It is worth considering the order of magnitude of $\Delta\theta$ representing the temperature fronts, despite the sensitivities discussed above for the precise values. The average vertical gradient of temperature across the front in Fig. 11d increases from approximately 0.06 K m^{-1} for $z_i/L = 1.7$ to 0.2 K m^{-1} for $z_i/L = 6$. Both values are significantly larger than the capping inversion (0.01 K m^{-1}). In contrast, the primary vertical motions associated with roller modes, bursting events, and downward sweeps are proportional to u_* , which decreases with increasing stratification. Future research into the dynamics of these features may reveal that the vertical motions are relatively unrestricted within the uniform zones but are unable to penetrate the large density gradients of the local fronts under strong stability, leading to reduced vertical mixing by turbulence and enhanced layering in flow realizations. The instantaneous flow structure and strong local thermal inversions play a central role in this phenomenological picture, which differs from the traditional view that eddies in the stable PBL lose kinetic energy by acting against the relatively weaker mean temperature gradient.

Findings related to the uniform zone size are specific to the vertical thickness, as the horizontal extent of eddies is not quantified here. Figure 4 provides visual evidence that the turbulent fluctuations lose coherence in the along-wind direction as stratification increases, i.e., they become less “streaky”. However, coherence in the fluctuations is retained at the scale of the local flow volume $\mathcal{L}_{x',y}$ used for the zone detection such that the uniform zone signature is present for each case. For neutral boundary layers, multiple UMZs and associated vortical features are often aligned along the extent of the largest motions (see, e.g., Adrian et al. 2000; Marusic 2001; Hwang and Sung 2018). Figure 4 suggests that stratification disrupts the largest motions and the alignment of UMZs which leads to a deficit in turbulent energy at low wavenumbers (Kaimal et al. 1972), but the individual zones corresponding to the production scales remain present, at least for the range of stability simulated. Further investigation is required to corroborate these observations.

The present analysis of UMZs and UTZs provides a more concrete description for the organization of turbulent eddies in the stable PBL and how these eddies are related to mean flow properties. It is possible that a similar organization of relatively uniform regions and thin gradient layers is present for more complex flow conditions such as in the presence of wave effects, in the roughness layer of canopies, or around complex terrain, to name a few. However, the persistent orientation of these features into distinct layers may be a specific property of shear-driven and stratified turbulent flows. Future studies must determine whether the zonal approximation of the instantaneous turbulent flow is applicable to these complex scenarios.

Acknowledgements M.H. is financially supported by the US National Science Foundation (NSF-AGS-2031312). The authors gratefully acknowledge the National Center for Atmospheric Research Computational Information Systems Laboratory for computing resources related to the original simulations (<http://n2t.net/ark:/85065/d7wd3xhc>) and post-processing analysis ([doi:10.5065/D6RX99HX](https://doi.org/10.5065/D6RX99HX)).

Data Availability Statistics for the uniform zones are available from the Dryad data repository: <https://doi.org/10.5068/D1TX0T>. Sample MATLAB scripts for detecting uniform zones are available from a separate Zenodo repository: <https://doi.org/10.5281/zenodo.7269145>. Additional data and code inquiries should be directed to the corresponding author.

Declarations

Conflict of interest The authors have no competing interests to declare.

Open Access This article is licensed under a Creative Commons Attribution 4.0 International License, which permits use, sharing, adaptation, distribution and reproduction in any medium or format, as long as you give appropriate credit to the original author(s) and the source, provide a link to the Creative Commons licence, and indicate if changes were made. The images or other third party material in this article are included in the article's Creative Commons licence, unless indicated otherwise in a credit line to the material. If material is not included in the article's Creative Commons licence and your intended use is not permitted by statutory regulation or exceeds the permitted use, you will need to obtain permission directly from the copyright holder. To view a copy of this licence, visit <http://creativecommons.org/licenses/by/4.0/>.

References

- Adrian RJ (2007) Hairpin vortex organization in wall turbulence. *Phys Fluids* 19(041):301. <https://doi.org/10.1063/1.2717527>
- Adrian RJ, Meinhardt CD, Tomkins CD (2000) Vortex organization in the outer region of the turbulent boundary layer. *J Fluid Mech* 422:1–54. <https://doi.org/10.1017/S0022112000001580>
- Antonia RA, Chambers AJ, Friehe CA, van Atta CW (1979) Temperature ramps in the atmospheric surface layer. *J Atmos Sci* 36(1):99–108. [https://doi.org/10.1175/1520-0469\(1979\)036<0099:TRITAS>2.0.CO;2](https://doi.org/10.1175/1520-0469(1979)036<0099:TRITAS>2.0.CO;2)
- Atkinson BW, Zhang JW (1996) Mesoscale shallow convection in the atmosphere. *Rev Geophys* 34(4):403–431. <https://doi.org/10.1029/96RG02623>
- Atoufi A, Scott KA, Waite ML (2021) Kinetic energy cascade in stably stratified open-channel flows. *J Fluid Mech* 925:A25. <https://doi.org/10.1017/jfm.2021.665>
- Basak S, Sarkar S (2006) Dynamics of a stratified shear layer with horizontal shear. *J Fluid Mech* 568:19–54. <https://doi.org/10.1017/S0022112006001686>
- Basu S, Porté-Agel F (2006) Large-eddy simulation of stably stratified atmospheric boundary layer turbulence: a scale-dependent dynamic modeling approach. *J Atmos Sci* 63(8):2074–2091. <https://doi.org/10.1175/JAS3734.1>
- Batchelor GK, Townsend AA (1949) The nature of turbulent motion at large wave-numbers. *Proc R Soc A* 199(1057):238–255. <https://doi.org/10.1098/rspa.1949.0136>
- Bautista JCC, Ebadi A, White CM, Chini GP, Klewicki JC (2019) A uniform momentum zone-vortical fissure model of the turbulent boundary layer. *J Fluid Mech* 858:609–633. <https://doi.org/10.1017/jfm.2018.769>
- Beare RJ, Macvean MK, Holtslag AAM, Cuxart J, I E, Golaz JC, Jimenez MA, Khairoutdinov M, Kosovic B, Lewellen D, Lund TS, Lundquist JK, McCabe A, Moene AF, Noh Y, Raasch S, Sullivan PP. (2006) An intercomparison of large-eddy simulations of the stable boundary layer. *Boundary-Layer Meteorol* 118(2):247–272. <https://doi.org/10.1007/s10546-004-2820-6>
- Blackadar AK (1957) Boundary layer wind maxima and their significance for the growth of nocturnal inversions. *Bull Amer Meteor Soc* 38(5):283–290. <https://doi.org/10.1175/1520-0477-38.5.283>
- Blackadar AK (1962) The vertical distribution of wind and turbulent exchange in a neutral atmosphere. *J Geophys Res* 67(8):3095–3102. <https://doi.org/10.1029/JZ067i008p03095>
- Bose ST, Park GI (2018) Wall-modeled large eddy simulation for complex turbulent flows. *Annu Rev Fluid Mech* 50:535–561. <https://doi.org/10.1146/annurev-fluid-122316-045241>
- Bou-Zeid E, Gao X, Ansong C, Katul GG (2018) On the role of return to isotropy in wall-bounded turbulent flows with buoyancy. *J Fluid Mech* 856:61–78. <https://doi.org/10.1017/jfm.2018.693>
- Buaría D, Pumir A, Bodenschatz E, Yeung PK (2019) Extreme velocity gradients in turbulent flows. *New J Phys* 21(043):004. <https://doi.org/10.1088/1367-2630/ab0756>

- Businger JA, Wyngaard JC, Izumi Y, Bradley EF (1971) Flux-profile relationships in the atmospheric surface layer. *J Atmos Sci* 28(2):181–189. [https://doi.org/10.1175/1520-0469\(1971\)028<0181:FPRITA>2.0.CO;2](https://doi.org/10.1175/1520-0469(1971)028<0181:FPRITA>2.0.CO;2)
- Carper M, Porté-Agel F (2004) The role of coherent structures in subfilter-scale dissipation of turbulence measured in the atmospheric surface layer. *J Turbul* 5:N40. <https://doi.org/10.1088/1468-5248/5/1/040>
- Caulfield CP (2021) Layering, instabilities, and mixing in turbulent stratified flows. *Annu Rev Fluid Mech* 53:113–145. <https://doi.org/10.1146/annurev-fluid-042320-100458>
- Chamecki M, Dias NL, Salesky ST, Pan Y (2017) Scaling laws for the longitudinal structure function in the atmospheric surface layer. *J Atmos Sci* 74(4):1127–1147. <https://doi.org/10.1175/JAS-D-16-0228.1>
- Chamecki M, Freire LS, Dias NL, Chen B, Dias-Junior CQ, Toledo Machado LA, Sörgel M, Tsokankunku A, de Araújo AC (2020) Effects of vegetation and topography on the boundary layer structure above the Amazon forest. *J Atmos Sci* 77(8):2941–2957. <https://doi.org/10.1175/JAS-D-20-0063.1>
- Chauhan K, Hutchins N, Monty J, Marusic I (2013) Structure inclination angles in the convective atmospheric surface layer. *Boundary-Layer Meteorol* 147:41–50. <https://doi.org/10.1007/s10546-012-9777-7>
- Chen CHP, Blackwelder RF (1978) Large-scale motion in a turbulent boundary layer: a study using temperature contamination. *J Fluid Mech* 89(1):1–31. <https://doi.org/10.1017/S0022112078002438>
- Chinita MJ, Matheou G, Miranda PMA (2022) Large-eddy simulation of very stable boundary layers. Part II: Length scales and anisotropy in stratified atmospheric turbulence. *Q J R Meteorol Soc* 148(745):1824–1839. <https://doi.org/10.1002/qj.4280>
- Chung D, Matheou G (2012) Direct numerical simulation of stationary homogeneous stratified sheared turbulence. *J Fluid Mech* 696:434–467. <https://doi.org/10.1017/jfm.2012.59>
- Cuxart J, Holtslag AAM, Beare RJ, Bazile E, Beljaars A, Cheng A, Conangla L, Ek M, Freedman F, Hamdi R, Kerstein A, Kitigawa H, Lenderink G, Lewellen D, Mailhot J, Mauritsen T, Perov V, Schayes G, Steeneveldt G, Svensson G, Taylor P, Weng W, Wunsch W, Xu KM (2006) Single-column model inter-comparison for a stably stratified atmospheric boundary layer. *Boundary-Layer Meteorol* 118:273–303. <https://doi.org/10.1007/s10546-005-3780-1>
- Davidson PA, Krogstad PÅ (2014) A universal scaling for low-order structure functions in the log-law region of smooth- and rough-wall boundary layers. *J Fluid Mech* 752:140–156. <https://doi.org/10.1017/jfm.2014.286>
- de Silva CM, Hutchins N, Marusic I (2016) Uniform momentum zones in turbulent boundary layers. *J Fluid Mech* 786:309–331. <https://doi.org/10.1017/jfm.2015.672>
- de Silva CM, Philip J, Hutchins N, Marusic I (2017) Interfaces of uniform momentum zones in turbulent boundary layers. *J Fluid Mech* 820:451–478. <https://doi.org/10.1017/jfm.2017.197>
- Delage Y (1974) A numerical study of the nocturnal atmospheric boundary layer. *Q J Roy Meteorol Soc* 100(425):351–364. <https://doi.org/10.1002/qj.49710042507>
- Dennis DJ, Nickels TB (2011) Experimental measurement of large-scale three-dimensional structures in a turbulent boundary layer. Part 1: Vortex packets. *J Fluid Mech* 673:180–217. <https://doi.org/10.1017/S0022112010006324>
- Dyer AJ (1974) A review of flux-profile relationships. *Boundary-Layer Meteorol* 7:363–372. <https://doi.org/10.1007/BF00240838>
- Ebadi A, Bautista JCC, White CM, Chini GP, Klewicki JC (2020) A heat transfer model of fully developed turbulent channel flow. *J Fluid Mech* 884:R7. <https://doi.org/10.1017/jfm.2019.1006>
- Eisma J, Westerweel J, Ooms G, Elsinga GE (2015) Interfaces and internal layers in a turbulent boundary layer. *Phys Fluids* 27(5):055,103. <https://doi.org/10.1063/1.4919909>
- Elsinga GE, Ishihara T, Hunt JCR (2020) Extreme dissipation and intermittency in turbulence at very high Reynolds numbers. *Proc R Soc A* 476(2243):20200,591. <https://doi.org/10.1098/rspa.2020.0591>
- Elsinga GE, Marusic I (2010) Universal aspects of small-scale motions in turbulence. *J Fluid Mech* 662:514–539. <https://doi.org/10.1017/S0022112010003381>
- Etling D, Brown RA (1993) Roll vortices in the planetary boundary layer?: A review. *Boundary-Layer Meteorol* 65:215–248. <https://doi.org/10.1007/BF00705527>
- Fan D, Xu J, Yao MX, Hickey JP (2019) On the detection of internal interfacial layers in turbulent flows. *J Fluid Mech* 872:198–217. <https://doi.org/10.1017/jfm.2019.343>
- Foken T (2006) 50 years of the Monin-Obukhov similarity theory. *Boundary-Layer Meteorol* 119:431–447. <https://doi.org/10.1007/s10546-006-9048-6>
- Frisch U, Sulem PL, Nelkin M (1978) A simple dynamical model of intermittent fully developed turbulence. *J Fluid Mech* 87(4):719–736. <https://doi.org/10.1017/S0022112078001846>
- García-Villalba M, del Álamo JC (2011) Turbulence modification by stable stratification in channel flow. *Phys Fluids* 23(4):045,104. <https://doi.org/10.1063/1.3560359>

- Ghannam K, Katul GG, Bou-Zeid E, Gerken T, Chamecki M (2018) Scaling and similarity of the anisotropic coherent eddies in near-surface atmospheric turbulence. *J Atmos Sci* 75(3):943–964. <https://doi.org/10.1175/JAS-D-17-0246.1>
- Glazunov AV, Mortikov EV, Barskov KV, Kadantsev EV, Zilitinkevich SS (2019) Layered structure of stably stratified turbulent shear flows. *Izv Atmos Ocean Phys* 55:312–323. <https://doi.org/10.1134/S0001433819040042>
- Grachev AA, Andreas EL, Fairall CW, Guest PS, Persson POG (2013) The critical Richardson number and limits of applicability of local similarity theory in the stable boundary layer. *Boundary-Layer Meteorol* 147:51–82. <https://doi.org/10.1007/s10546-012-9771-0>
- Gul M, Elsinga GE, Westerweel J (2020) Internal shear layers and edges of uniform momentum zones in a turbulent pipe flow. *J Fluid Mech* 901:A10. <https://doi.org/10.1017/jfm.2020.503>
- Hartogensis OK, de Bruin HAR (2005) Monin-Obukhov similarity functions of the structure parameter of temperature and turbulent kinetic energy dissipation rate in the stable boundary layer. *Boundary-Layer Meteorol* 116:253–276. <https://doi.org/10.1007/s10546-004-2817-1>
- Heisel M, Dasari T, Liu Y, Hong J, Coletti F, Guala M (2018) The spatial structure of the logarithmic region in very-high-Reynolds-number rough wall turbulent boundary layers. *J Fluid Mech* 857:704–747. <https://doi.org/10.1017/jfm.2018.759>
- Heisel M, Katul GG, Chamecki M, Guala M (2020) Velocity asymmetry and turbulent transport closure in smooth- and rough-wall boundary layers. *Phys Rev Fluids* 5(104):605. <https://doi.org/10.1103/PhysRevFluids.5.104605>
- Heisel M, de Silva CM, Hutchins N, Marusic I, Guala M (2020) On the mixing length eddies and logarithmic mean velocity profile in wall turbulence. *J Fluid Mech* 887:R1. <https://doi.org/10.1017/jfm.2020.23>
- Heisel M, de Silva CM, Hutchins N, Marusic I, Guala M (2021) Prograde vortices, internal shear layers and the Taylor microscale in high-Reynolds-number wall turbulence. *J Fluid Mech* 920:A52. <https://doi.org/10.1017/jfm.2021.478>
- Heisel M, de Silva CM, Katul GG, Chamecki M (2022) Self-similar geometries within the inertial subrange of scales in boundary layer turbulence. *J Fluid Mech* 942:A33. <https://doi.org/10.1017/jfm.2022.409>
- Högström ULF (1988) Non-dimensional wind and temperature profiles in the atmospheric surface layer: A re-evaluation. *Boundary-Layer Meteorol* 42:55–78. <https://doi.org/10.1007/BF00119875>
- Holtislag AAM, Nieuwstadt FTM (1986) Scaling the atmospheric boundary layer. *Boundary-Layer Meteorol* 36:201–209. <https://doi.org/10.1007/BF00117468>
- Hommema SE, Adrian RJ (2003) Packet structure of surface eddies in the atmospheric boundary layer. *Boundary-Layer Meteorol* 106:147–170. <https://doi.org/10.1023/A:1020868132429>
- Huang J, Bou-Zeid E (2013) Turbulence and vertical fluxes in the stable atmospheric boundary layer. Part I: A large-eddy simulation study. *J Atmos Sci* 70(6):1513–1527. <https://doi.org/10.1175/JAS-D-12-0167.1>
- Huang J, Bou-Zeid E, Golaz JC (2013) Turbulence and vertical fluxes in the stable atmospheric boundary layer. Part II: A novel mixing-length model. *J Atmos Sci* 70(6):1528–1542. <https://doi.org/10.1175/JAS-D-12-0168.1>
- Hunt JCR, Eames I, Westerweel J, Davidson PA, Voropayev S, Fernando J, Braza M (2010) Thin shear layers - the key to turbulence structure? *J Hydro-environ Res* 94(2):75–82. <https://doi.org/10.1016/j.jher.2010.04.010>
- Hunt JCR, Ishihara T, Worth NA, Kaneda Y (2014) Thin shear layer structures in high Reynolds number turbulence. *Flow Turbul Combust* 92(3):607–649. <https://doi.org/10.1007/s10494-013-9518-0>
- Hutchins N, Marusic I (2007) Evidence of very long meandering features in the logarithmic region of turbulent boundary layers. *J Fluid Mech* 579:1–28. <https://doi.org/10.1017/S0022112006003946>
- Hutchins N, Chauhan K, Marusic I, Monty JP, Klewicki JC (2012) Towards reconciling the large-scale structure of turbulent boundary layers in the atmosphere and laboratory. *Boundary-Layer Meteorol* 145(2):273–306. <https://doi.org/10.1007/s10546-012-9735-4>
- Hwang J, Sung HJ (2018) Wall-attached structures of velocity fluctuations in a turbulent boundary layer. *J Fluid Mech* 856:958–983. <https://doi.org/10.1017/jfm.2018.759>
- Ishihara T, Gotoh T, Kaneda Y (2009) Study of high-Reynolds number isotropic turbulence by direct numerical simulation. *Annu Rev Fluid Mech* 41(1):165–180. <https://doi.org/10.1146/annurev.fluid.010908.165203>
- Ishihara T, Kaneda Y, Hunt JCR (2013) Thin shear layers in high Reynolds number turbulence - DNS results. *Flow Turbul Combust* 91(4):895–929. <https://doi.org/10.1007/s10494-013-9499-z>
- Jayaraman B, Brasseur JG (2021) Transition in atmospheric boundary layer turbulence structure from neutral to convective, and large-scale rolls. *J Fluid Mech* 913:A42. <https://doi.org/10.1017/jfm.2021.3>
- Jiménez J (2018) Coherent structures in wall-bounded turbulence. *J Fluid Mech* 842:P1. <https://doi.org/10.1017/jfm.2018.144>
- Kaimal JC, Wyngaard JC, Izumi Y, Coté OR (1972) Spectral characteristics of surface-layer turbulence. *Q J Roy Meteor Soc* 98(417):563–589. <https://doi.org/10.1002/qj.49709841707>

- Katul GG, Konings AG, Porporato A (2011) Mean velocity profile in a sheared and thermally stratified atmospheric boundary layer. *Phys Rev Lett* 107(268):502. <https://doi.org/10.1103/PhysRevLett.107.268502>
- Kays WM (1994) Turbulent Prandtl number-Where are we? *J Heat Transfer* 116(2):284–295. <https://doi.org/10.1115/1.2911398>
- Khanna S, Brasseur JG (1998) Three-dimensional buoyancy- and shear-induced local structure of the atmospheric boundary layer. *J Atmos Sci* 55(5):710–743. [https://doi.org/10.1175/1520-0469\(1998\)055<0710:TDBASI>2.0.CO;2](https://doi.org/10.1175/1520-0469(1998)055<0710:TDBASI>2.0.CO;2)
- Kikuchi T, Chiba O (1985) Step-like temperature fluctuations associated with inverted ramps in a stable surface layer. *Boundary-Layer Meteorol* 31:51–63. <https://doi.org/10.1007/BF00120034>
- Kolmogorov AN (1962) A refinement of previous hypotheses concerning the local structure of turbulence in a viscous incompressible fluid at high reynolds number. *J Fluid Mech* 13(1):82–85. <https://doi.org/10.1017/S0022112062000518>
- Kosović B, Curry JA (2000) A large eddy simulation study of a quasi-steady, stably stratified atmospheric boundary layer. *J Atmos Sci* 57(8):1052–1068. [https://doi.org/10.1175/1520-0469\(2000\)057<1052:ALESSO>2.0.CO;2](https://doi.org/10.1175/1520-0469(2000)057<1052:ALESSO>2.0.CO;2)
- Krug D, Lohse D, Stevens RJAM (2020) Coherence of temperature and velocity superstructures in turbulent Rayleigh-Bénard flow. *J Fluid Mech* 887:A2. <https://doi.org/10.1017/jfm.2019.1054>
- Lan C, Liu H, Li D, Katul GG, Finn D (2018) Distinct turbulent structures in stably stratified boundary layers with weak and strong surface shear. *J Geophys Res* 123(15):7839–7854. <https://doi.org/10.1029/2018JD028628>
- Larsson J, Kawai S, Bodart J, Bermejo-Moreno I (2015) Large eddy simulation with modeled wall-stress: recent progress and future directions. *Mech Eng Rev* 3:1–23. <https://doi.org/10.1299/mer.15-00418>
- Laskari A, de Kat R, Hearst RJ, Ganapathisubramani B (2018) Time evolution of uniform momentum zones in a turbulent boundary layer. *J Fluid Mech* 842:554–590. <https://doi.org/10.1017/jfm.2018.126>
- Li D (2019) Turbulent Prandtl number in the atmospheric boundary layer - where are we now? *Atmos Res* 216:86–105. <https://doi.org/10.1016/j.atmosres.2018.09.015>
- Lin CL, McWilliams JC, Moeng CH, Sullivan PP (1996) Coherent structures and dynamics in a neutrally stratified planetary boundary layer flow. *Phys Fluids* 8(10):2626–2639. <https://doi.org/10.1063/1.869048>
- Liu HY, Bo TL, Liang YR (2017) The variation of large-scale structure inclination angles in high Reynolds number atmospheric surface layers. *Phys Fluids* 29(035):104. <https://doi.org/10.1063/1.4978803>
- Mahrt L (1989) Intermittency of atmospheric turbulence. *J Atmos Sci* 46(1):79–95. [https://doi.org/10.1175/1520-0469\(1989\)046<0079:IOAT>2.0.CO;2](https://doi.org/10.1175/1520-0469(1989)046<0079:IOAT>2.0.CO;2)
- Mahrt L (1999) Stratified atmospheric boundary layers. *Boundary-Layer Meteorol* 90:375–396. <https://doi.org/10.1023/A:1001765727956>
- Mahrt L (2014) Stably stratified atmospheric boundary layers. *Annu Rev Fluid Mech* 46:23–45. <https://doi.org/10.1146/annurev-fluid-010313-141354>
- Mahrt L (2019) Microfronts in the nocturnal boundary layer. *Q J Roy Meteorol Soc* 145(719):546–562. <https://doi.org/10.1002/qj.3451>
- Mahrt L, Howell J (1994) The influence of coherent structures and microfronts on scaling laws using global and local transforms. *J Fluid Mech* 260:247–270. <https://doi.org/10.1017/S0022112094003502>
- Marusic I (2001) On the role of large-scale structures in wall turbulence. *Phys Fluids* 13(3):735–743. <https://doi.org/10.1063/1.1343480>
- Marusic I, Monty JP (2019) Attached eddy model of wall turbulence. *Annu Rev Fluid Mech* 51:49–74. <https://doi.org/10.1146/annurev-fluid-010518-040427>
- Mason PJ, Thomson DJ (1992) Stochastic backscatter in large-eddy simulations of boundary layers. *J Fluid Mech* 242:51–78. <https://doi.org/10.1017/S0022112092002271>
- Matheou G, Chung D (2014) Large-eddy simulation of stratified turbulence. Part II: Application of the stretched-vortex model to the atmospheric boundary layer. *J Atmos Sci* 71(12):4439–4460. <https://doi.org/10.1175/JAS-D-13-0306.1>
- Meinhart CD, Adrian RJ (1995) On the existence of uniform momentum zones in a turbulent boundary layer. *Phy Fluids* 7(4):694–696. <https://doi.org/10.1063/1.868594>
- Meneveau CM, Sreenivasan KR (1991) The multifractal nature of turbulent energy dissipation. *J Fluid Mech* 224:429–484. <https://doi.org/10.1017/S0022112091001830>
- Mironov DV, Sullivan PP (2016) Second-moment budgets and mixing intensity in the stably stratified atmospheric boundary layer over thermally heterogeneous surfaces. *J Atmos Sci* 73(1):449–464. <https://doi.org/10.1175/JAS-D-15-0075.1>
- Moeng CH (1984) A large-eddy-simulation model for the study of planetary boundary-layer turbulence. *J Atmos Sci* 41(13):2052–2062. [https://doi.org/10.1175/1520-0469\(1984\)041<2052:ALESMT>2.0.CO;2](https://doi.org/10.1175/1520-0469(1984)041<2052:ALESMT>2.0.CO;2)

- Moeng CH, Sullivan PP (1994) A comparison of shear- and buoyancy-driven planetary boundary layer flows. *J Atmos Sci* 51(7):999–1022. [https://doi.org/10.1175/1520-0469\(1994\)051<0999:ACOSAB>2.0.CO;2](https://doi.org/10.1175/1520-0469(1994)051<0999:ACOSAB>2.0.CO;2)
- Moeng CH, Wyngaard JC (1988) Spectral analysis of large-eddy simulations of the convective boundary layer. *J Atmos Sci* 45(23):3573–3587. [https://doi.org/10.1175/1520-0469\(1988\)045<3573:SAOLES>2.0.CO;2](https://doi.org/10.1175/1520-0469(1988)045<3573:SAOLES>2.0.CO;2)
- Monin AS, Obukhov AM (1954) Basic laws of turbulent mixing in the atmosphere near the ground. *Trudy Akad Nauk SSSR Geophiz Inst* 24(151):163–187
- Nieuwstadt FTM (1984) The turbulent structure of the stable, nocturnal boundary layer. *J Atmos Sci* 41(14):2202–2216. [https://doi.org/10.1175/1520-0469\(1984\)041<2202:TTSOTS>2.0.CO;2](https://doi.org/10.1175/1520-0469(1984)041<2202:TTSOTS>2.0.CO;2)
- Obukhov AM (1946) Turbulence in an atmosphere with a non-uniform temperature. *Trudy Inst Theor Geofiz AN SSSR* 1:95–115
- Obukhov AM (1962) Some specific features of atmospheric turbulence. *J Fluid Mech* 13(1):77–81. <https://doi.org/10.1017/S0022112062000506>
- Patton EG, Sullivan PP, Shaw RH, Finnigan JJ, Weil JC (2016) Atmospheric stability influences on coupled boundary layer and canopy turbulence. *J Atmos Sci* 73(4):1621–1647. <https://doi.org/10.1175/JAS-D-15-0068.1>
- Pope SB (2000) *Turbulent Flows*, 1st edn. Cambridge University Press
- Prandtl L (1932) Zur turbulenten strömung in röhren und längs platten. *Ergebn Aerodyn Versuchsanst* 4:18–29
- Praud O, Fincham AM, Sommeria J (2005) Decaying grid turbulence in a strongly stratified fluid. *J Fluid Mech* 522:1–33. <https://doi.org/10.1017/S002211200400120X>
- Priyadarshana PJA, Klewicki JC, Treat S, Foss JF (2007) Statistical structure of turbulent-boundary-layer velocity-vorticity products at high and low Reynolds numbers. *J Fluid Mech* 570:307–346. <https://doi.org/10.1017/S0022112006002771>
- Salesky ST, Katul GG, Chamecki M (2013) Buoyancy effects on the integral lengthscales and mean velocity profile in atmospheric surface layer flows. *Phys Fluids* 25(10):105,101, <https://doi.org/10.1063/1.4823747>
- Salesky ST, Anderson W (2018) Buoyancy effects on large-scale motions in convective atmospheric boundary layers: implications for modulation of near-wall processes. *J Fluid Mech* 856:135–168. <https://doi.org/10.1017/jfm.2018.711>
- Salesky ST, Chamecki M, Bou-Zeid E (2017) On the nature of the transition between roll and cellular organization in the convective boundary layer. *Boundary-Layer Meteorol* 163:41–68. <https://doi.org/10.1007/s10546-016-0220-3>
- Shah S, Bou-Zeid E (2014) Very-large-scale motions in the atmospheric boundary layer educed by snapshot proper orthogonal decomposition. *Boundary-Layer Meteorol* 153:355–387. <https://doi.org/10.1007/s10546-014-9950-2>
- Smits AJ, McKeon BJ, Marusic I (2011) High-Reynolds number wall turbulence. *Annu Rev Fluid Mech* 43(1):353–375. <https://doi.org/10.1146/annurev-fluid-122109-160753>
- Sorbjan Z (1986) On similarity in the atmospheric boundary layer. *Boundary-Layer Meteorol* 34:377–397. <https://doi.org/10.1007/BF00120989>
- Sreenivasan KR, Antonia RA (1997) The phenomenology of small-scale turbulence. *Annu Rev Fluid Mech* 29:435–472. <https://doi.org/10.1146/annurev.fluid.29.1.435>
- Stull RB (1988) *An Introduction to Boundary Layer Meteorology*. Kluwer Academic Publishers. <https://doi.org/10.1007/978-94-009-3027-8>
- Sullivan PP, McWilliams JC, Moeng CH (1994) A subgrid-scale model for large-eddy simulation of planetary boundary-layer flows. *Boundary-Layer Meteorol* 71:247–276. <https://doi.org/10.1007/BF00713741>
- Sullivan PP, Moeng CH, Stevens B, Lenschow DH, Mayor SD (1998) Structure of the entrainment zone capping the convective atmospheric boundary layer. *J Atmos Sci* 55(19):3042–3064. [https://doi.org/10.1175/1520-0469\(1998\)055<3042:SOTEZC>2.0.CO;2](https://doi.org/10.1175/1520-0469(1998)055<3042:SOTEZC>2.0.CO;2)
- Sullivan PP, Weil JC, Patton EG, Jonker HJJ, Mironov DV (2016) Turbulent winds and temperature fronts in large-eddy simulations of the stable atmospheric boundary layer. *J Atmos Sci* 73(4):1815–1840. <https://doi.org/10.1175/JAS-D-15-0339.1>
- Townsend AA (1976) *The Structure of Turbulent Shear Flow*, 2nd edn. Cambridge University Press
- Träumner K, Damian T, Stawiarski C, Wieser A (2015) Turbulent structures and coherence in the atmospheric surface layer. *Boundary-Layer Meteorol* 154:1–25. <https://doi.org/10.1007/s10546-014-9967-6>
- Waite ML (2011) Stratified turbulence at the buoyancy scale. *Phys Fluids* 23(6):066,602, <https://doi.org/10.1063/1.3599699>
- Warhaft Z (2000) Passive scalars in turbulent flows. *Annu Rev Fluid Mech* 32:203–240. <https://doi.org/10.1146/annurev.fluid.32.1.203>

- Watanabe T, Riley JJ, Nagata K, Matsuda K, Onishi R (2019) Hairpin vortices and highly elongated flow structures in a stably stratified shear layer. *J Fluid Mech* 878:37–61. <https://doi.org/10.1017/jfm.2019.577>
- Wilczak JM, Tillman JE (1980) The three-dimensional structure of convection in the atmospheric surface layer. *J Atmos Sci* 37(11):2424–2443. [https://doi.org/10.1175/1520-0469\(1980\)037<2424:TTDSOC>2.0.CO;2](https://doi.org/10.1175/1520-0469(1980)037<2424:TTDSOC>2.0.CO;2)
- Wyngaard JC (1992) Atmospheric turbulence. *Annu Rev Fluid Mech* 24:205–234. <https://doi.org/10.1146/annurev.fl.24.010192.001225>
- Wyngaard JC, Coté OR (1972) Cospectral similarity in the atmospheric surface layer. *Q J R Meteorol Soc* 98(417):590–603. <https://doi.org/10.1002/qj.49709841708>
- Wyngaard JC, Seaman N, Kimmel SJ, Otte M, Di X, Gilbert KE (2001) Concepts, observations, and simulation of refractive index turbulence in the lower atmosphere. *Radio Sci* 36(4):643–669. <https://doi.org/10.1029/2000RS002380>
- Yamada T (1975) The critical Richardson number and the ratio of the eddy transport coefficients obtained from a turbulence closure model. *J Atmos Sci* 32(5):926–933. [https://doi.org/10.1175/1520-0469\(1975\)032<0926:TCRNAT>2.0.CO;2](https://doi.org/10.1175/1520-0469(1975)032<0926:TCRNAT>2.0.CO;2)
- Young GS, Kristovich DAR, Hjelmfelt MR, Foster RC (2002) Rolls, streets, waves, and more. *Bull Amer Meteor Soc* 83(7):997–1002. [https://doi.org/10.1175/1520-0477\(2002\)083<0997:RSWAMA>2.3.CO;2](https://doi.org/10.1175/1520-0477(2002)083<0997:RSWAMA>2.3.CO;2)

Publisher's Note Springer Nature remains neutral with regard to jurisdictional claims in published maps and institutional affiliations.